Journal of Computational Physics **171,** 289–335 (2001)
doi:10.1006/jcph.2001.6790, available online at http://www.idealibrary.com on IDEAL®

A Gas-Kinetic BGK Scheme for the Navier–Stokes Equations and Its Connection with Artificial Dissipation and Godunov Method[1]

Kun Xu

Mathematics Department, Hong Kong University of Science and Technology, Clear Water Bay, Kowloon, Hong Kong
E-mail: makxu@uxmail.ust.hk

Received August 23, 2000; revised March 26, 2001

This paper presents an improved gas-kinetic scheme based on the Bhatnagar–Gross–Krook (BGK) model for the compressible Navier–Stokes equations. The current method extends the previous gas-kinetic Navier–Stokes solver developed by Xu and Prendergast (*J. Comput. Phys.* **114**, 9) by (a) implementing a general nonequilibrium state based on the Chapman–Enskog expansion of the BGK model as the initial gas distribution function at each time step, (b) using a different way in the construction of the equilibrium state at a cell interface, and (c) keeping two slopes of the macroscopic variables in the evaluation of spatial variations of the equilibrium state. As a result, the previous requirement of particle collision time τ being less than the time step Δt for the validity of the BGK Navier–Stokes solver is removed, and the scheme becomes more robust than the previous one. The current BGK method approximates the Navier–Stokes solutions accurately regardless of the ratio between the particle collision time and the numerical time step. The Kinetic Flux Vector Splitting Navier–Stokes (KFVS NS) solver developed by Chou and Baganoff comes to be the limiting case of the current method when the particle collision time is much larger than the time step. The Equilibrium Flux Method (EFM) of Pullin for the Euler equations is also a limiting case of the current method when the nonequilibrium part in the initial gas distribution function disappears and the collision time is much larger than the time step. The dissipative mechanism in the KFVS and many other FVS schemes is qualitatively analyzed from their relation with the BGK scheme. Also, in this paper, the appropriate implementation of boundary condition for the kinetic scheme, different limiting solutions, and the Prandtl number fix are presented. The connection among von Neumann and Richtmyer's artificial dissipation,

[1] This paper was presented as an invited lecture at First International Conference on Computational Fluid Dynamics, July 9–14, 2000, Kyoto, Japan.

0021-9991/01 $35.00

Godunov method, and the gas-kinetic BGK scheme is discussed, from which the two concepts of *dynamical* and *kinematical dissipation* are introduced. The principles for constructing accurate and robust numerical schemes for the compressible flow simulation are proposed. Many numerical tests, which include highly nonequilibrium case (i.e., Mach 10 shock structure) are included to validate the BGK scheme for the viscous solutions and to support the physical and numerical analysis for different schemes.

Key Words: Gas-kinetic Method, Navier–Stokes equations, Chapman–Enskog expansion, kinetic boundary condition, shock capturing schemes, Navier–Stokes shock structure.

1. INTRODUCTION

There are two main approaches for the numerical Navier–Stokes solution for the compressible flow (i.e., the upwinding scheme and central difference method). For the upwinding scheme, the Navier–Stokes equations are solved in two steps, which are the inviscid Euler step and the viscous step. The Euler solution is obtained based on an exact or approximate Riemann solver. For the viscous part, a central difference method is generally adapted [17, 39]. For the central difference scheme, additional artificial dissipation is usually required in the NS flow solver.

Based on the gas-kinetic theory, the Navier–Stokes equations can be derived from the Boltzmann equation using the Chapman–Enskog expansion. A Navier–Stokes solver can be theoretically obtained also by solving the Boltzmann equation, or the simplified collision models [2, 4]. In a gas-kinetic representation, all flow variables are moments of a single particle distribution function.

Since a gas distribution function contains both equilibrium and nonequilibrium properties of the gas flow, the inviscid and viscous terms are obtained simultaneously. Also, because of the particle-related nature, the kinetic method could possibly be extended to the near continuum regime to match with the Direct Simulation Monte Carlo (DSMC) method [24]. However, the above properties in the gas-kinetic equation do not guarantee that the gas-kinetic schemes should be superior to other schemes for the Navier–Stokes solutions. It depends highly on the ways of solving the Boltzmann equation. In many kinetic schemes, the free transport equation or the collisionless Boltzmann equation (i.e., $f_t + u f_x = 0$) is solved in the gas evolution stage for the flux evaluation. Then, the collision part, i.e., $f_t = Q(f, f)$, is implicity implemented inside each cell. Even though a nonequilibrium gas distribution function f can be used as the initial condition for the free transport equation [8], as discussed in the current paper, this kind of kinetic NS solver is valid only under the condition $\mu/p \gg \Delta t$, where μ is the dynamical viscosity coefficient, p is the pressure, and Δt is the numerical time step. With the introduction of an equivalent particle collision time τ, such as $\tau = \mu/p$, the above requirement becomes $\tau \gg \Delta t$. Note that for any viscosity coefficient μ, the corresponding particle collision time τ can be approximately obtained using simple kinetic models [22, 29]. Since the free transport mechanism introduces a numerical collision time Δt, which generates a numerical viscosity being proportional to it, i.e., $\mu_{num} \sim \Delta t$ [26], the condition $\tau \gg \Delta t$ means that the physical viscosity coefficient should be much larger than the numerical one in order to have an accurate Navier–Stokes solution. Although the above condition can be satisfied in the shock structure calculations, in many situations, such as in the laminar boundary layer resolved by a limited number

of grid points, the above requirement cannot be true. Even targeting to the inviscid Euler equations, the numerical dissipation $\mu_{num} \sim \Delta t$ is still existing in all KFVS-type schemes [27, 30, 32, 33]. It is certainly true that a high-order interpolation or a well-limited initial condition could partially release the dynamical deficiency in the above gas transport model, but it turns out that success of this kind of scheme depends crucially on the reconstruction procedure. One purpose of this paper is to distinguish the physical and numerical effects in a CFD method.

The BGK scheme differs from the above kinetic methods mainly on the inclusion of particle collisions in the gas evolution stage. Instead of solving the collisionless Boltzmann equation, a collisional BGK model is used in the flux evaluation, i.e., $f_t + uf_x = (g - f)/\tau$ [1]. As a result, the dissipation in the transport process is controlled by the collision time τ rather than the time step Δt. As analyzed previously [46, 52], the BGK scheme does give a good approximate Navier–Stokes solution in the cases where $\tau < \Delta t$. Under such a situation, the distribution function used in the flux evaluation goes automatically to a Chapman–Enskog expansion of the BGK equation. The current paper is about the extension of the early BGK scheme by including a more realistic nonequilibrium state as the initial condition at each time step. Therefore, the BGK NS solver becomes valid in both $\tau < \Delta t$ and $\tau > \Delta t$ cases, and the influence of time step Δt on the accuracy of the viscous solution is reduced to a minimal level. Also, in the current paper, the appropriate implementation of boundary condition and Prandtl number fix will be presented. As a result, the BGK scheme becomes valid for the realistic compressible flow equation with a variable Prandtl number. Many test cases, including the boundary layer and shock structure calculations, are presented to validate the current approach. The relation among the schemes based on the artificial dissipation, the Riemann solver, and the current kinetic approach, will be discussed, from which two concepts of *dynamical* and *kinematic* dissipation are introduced.

2. A BGK SCHEME

In order to construct a finite-volume gas-kinetic scheme, we need to get a time-dependent gas distribution function f at a cell interface, from which the numerical flux can be obtained.

2.1. *Initial Data Reconstruction and Its Underlying Dynamics*

Following van Leer's MUSCL idea [40], a numerical scheme is composed of an initial reconstruction stage followed by a dynamical evolution stage. For a finite volume method, at the beginning of each time step $t = 0$ only cell averaged mass, momentum, and energy densities are given. The implicit dissipative mechanism in the construction of this constant state inside each cell was analyzed in [48], where the process of kinetic energy being transferred into the thermal one was for the first time explicitly pointed out. For example, the averaging of two states inside a cell, such as that shown in Fig. 1, is always associated with a kinetic energy loss $\Delta E_k \sim (U_1 - U_2)^2$. Physically, besides heating the gas, this amount of energy should also do work to compress or rarefy the gases. But, numerically it totally goes to heat. Many spurious solutions in the shock capturing schemes, such as the post-shock oscillation, shock instability, sonic point glitch, as well as wall over-heating, are solely related to the above averaging dissipative mechanism [19, 49, 53].

For a high-resolution scheme, interpolation techniques are used to construct the subcell structure. Simple polynomials usually generate spurious oscillations if large gradients exist

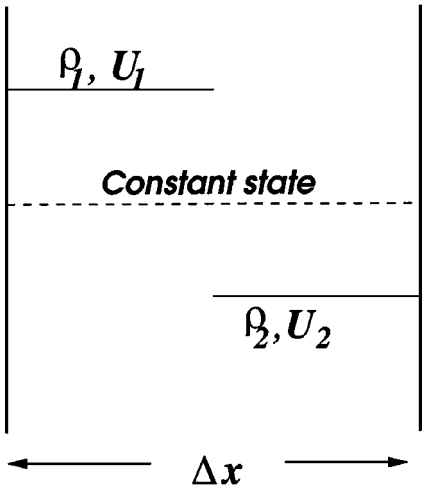

FIG. 1. The construction of a constant state inside each cell. The kinematic dissipation is introduced automatically through the averaging process [48].

in the data. The most successful interpolation techniques known so far are those based on the concepts of limiters [3, 40], and these interpolation rules can be applied to the conservative, characteristic, or primitive flow variables. In this paper, the reconstruction is solely applied to the conservative variables. The limiter used is the van Leer limiter. With the cell averaged conservative variables w_j, and their differences between neighboring cells $s_+ = (w_{j+1} - w_j)/\Delta x$ and $s_- = (w_j - w_{j-1})/\Delta x$, the slop of w in cell j is constructed as

$$L(s_+, s_-) = S(s_+, s_-)\frac{|s_+||s_-|}{|s_+| + |s_-|},$$

where $S(s_+, s_-) = \text{sign}(s_+) + \text{sign}(s_-)$. After reconstruction, the flow variable w is distributed linearly in cell j,

$$\bar{w}_j(x) = w_j + L(s_+, s_-)(x - x_j).$$

The interpolated flow distribution around a cell interface is shown in Fig. 2. The BGK

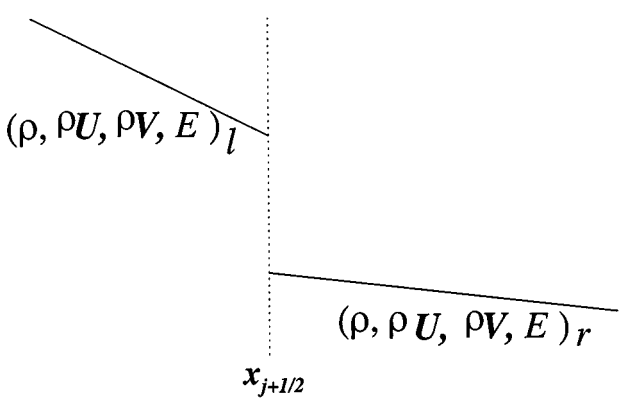

FIG. 2. The reconstructed initial conservative variables around a cell interface, from which the nonequilibrium state f_0 (8) is constructed. The BGK scheme is based on the solution of the collisional BGK model with the above initial condition.

scheme is basically to give a numerical Navier–Stokes solution locally under the above initial condition by capturing the time evolution of the gas distribution function.

For the first-order scheme, the construction of a constant state inside each cell introduces numerical dissipation with the coefficient $\nu_{num} \sim \Delta x$. Theoretically, a second-order interpolation will have $\nu_{num} \sim (\Delta x)^2$ in the smooth flow, but the coefficient in front of the dissipative term could depend sensitively on the limiters used. Even in the smooth region, it has been observed that the implementation of a nonlinear limiter, which slightly modifying the slopes up and down, could trigger bad convergence of a numerical scheme. For a highly nonequilibrium flow, such as the gas in the Mach 10 shock structure, the slight gradient change resulting from limiter could make a large difference in the solution, even destabilize the shock structure. So, in a well-resolved and highly nonequilibrium region, the nonlinear limiter could be harmful. The interpolations without using the limiter, such as the simple central difference,

$$\left.\frac{\partial \bar{w}}{\partial x}\right|_{j+1/2} = s_+, \quad \left.\frac{\partial \bar{w}}{\partial x}\right|_{j-1/2} = s_-, \tag{1}$$

will also be tested in some cases in the current paper.

2.2. *BGK Model and Viscous Equations*

In this section, a directional splitting method to solve the 2D BGK equation will be presented. The BGK model in the x-direction can be written as [22]

$$f_t + u f_x = \frac{g - f}{\tau}, \tag{2}$$

where f is the gas distribution function and g is the equilibrium state approached by f. Both f and g are functions of space x, time t, particle velocities (u, v), and internal variable ξ. The particle collision time τ is related to the viscosity and heat conduction coefficients. The equilibrium state is a Maxwellian distribution,

$$g = \rho\left(\frac{\lambda}{\pi}\right)^{\frac{K+2}{2}} e^{-\lambda((u-U)^2+(v-V)^2+\xi^2)},$$

where ρ is the density, U and V are the macroscopic velocities in the x- and y-directions, and $\lambda = m/2kT$, where m is the molecular mass, k is the Boltzmann constant, and T is the temperature. For a 2D flow with explicit account of U and V velocities, the random particle motion in the z direction is included into the internal variable ξ, and the total number of degrees of freedom K in ξ is equal to $(5 - 3\gamma)/(\gamma - 1) + 1$ [46]. For example, for a diatomic gas with $\gamma = 7/5$, K is equal to 3 to account for the particle motion in the z-direction and two rotational degrees of freedom. In the equilibrium state, the internal variable ξ^2 is equal to $\xi^2 = \xi_1^2 + \xi_2^2 + \cdots + \xi_K^2$. The relation between mass ρ, momentum $(n = \rho U, m = \rho V)$, and energy E densities with the distribution function f is

$$\begin{pmatrix} \rho \\ n \\ m \\ E \end{pmatrix} = \int \psi_\alpha f \, d\Xi, \quad \alpha = 1, 2, 3, 4, \tag{3}$$

where ψ_α is the component of the vector of moments

$$\psi = (\psi_1, \psi_2, \psi_3, \psi_4)^T = \left(1, u, v, \frac{1}{2}(u^2 + v^2 + \xi^2)\right)^T,$$

and $d\Xi = dudvd\xi$ is the volume element in the phase space with $d\xi = d\xi_1 d\xi_2 \cdots d\xi_K$. Since mass, momentum, and energy are conserved during particle collisions, f and g satisfy the conservation constraint,

$$\int (g - f)\psi_\alpha \, d\Xi = 0, \quad \alpha = 1, 2, 3, 4, \tag{4}$$

at any point in space and time. For an easy reference, the moments of a Maxwellian are given in Appendix A. In this paper, only a directional splitting BGK scheme is presented. A multidimensional BGK solver, which is defined as a scheme with the inclusion of flow gradients in both x- and y-directions, has to solve the 2D BGK model,

$$f_t + uf_x + vf_y = (g - f)/\tau.$$

A 2D BGK flow solver based on the above equation is proposed in [46, 52].

For a local equilibrium state with $f = g$, the Euler equations can be obtained by taking the moments of ψ_α to Eq. (2). This yields

$$\int \psi_\alpha (g_t + ug_x) \, d\Xi = 0, \quad \alpha = 1, 2, 3, 4,$$

and the corresponding Euler equations in the x-direction are

$$\begin{pmatrix} \rho \\ \rho U \\ \rho V \\ E \end{pmatrix}_t + \begin{pmatrix} \rho U \\ \rho U^2 + p \\ \rho UV \\ (E + p)U \end{pmatrix}_x = 0,$$

where $E = \frac{1}{2}\rho(U^2 + V^2 + \frac{K+2}{2\lambda})$ and $p = \rho/2\lambda$.

On the other hand, to the first order of τ, the Chapman–Enskog expansion gives $f = g - \tau(g_t + ug_x)$. Taking moments of ψ again to the BGK equation with the new f, we get

$$\int \psi (g_t + ug_x) \, d\Xi = \tau \int \psi (g_{tt} + 2ug_{xt} + u^2 g_{xx}) \, d\Xi,$$

from which the Navier–Stokes equations with a dynamic viscous coefficient $\mu = \tau p$ can be obtained,

$$\begin{pmatrix} \rho \\ \rho U \\ \rho V \\ E \end{pmatrix}_t + \begin{pmatrix} \rho U \\ \rho U^2 + p \\ \rho UV \\ (E + p)U \end{pmatrix}_x = \begin{pmatrix} 0 \\ s_{1x} \\ s_{2x} \\ s_{3x} \end{pmatrix}_x, \tag{5}$$

where

$$
\begin{aligned}
s_{1x} &= \tau p\left[2\frac{\partial U}{\partial x} - \frac{2}{K+2}\frac{\partial U}{\partial x}\right],\\
s_{2x} &= \tau p\frac{\partial V}{\partial x},\\
s_{3x} &= \tau p\left[2U\frac{\partial U}{\partial x} + V\frac{\partial V}{\partial x} - \frac{2}{K+2}U\frac{\partial U}{\partial x} + \frac{K+4}{4}\frac{\partial}{\partial x}\left(\frac{1}{\lambda}\right)\right].
\end{aligned}
$$

The full derivation of the Navier–Stokes equations for a monatomic gas from the BGK model in 3D case is given in [43]. For a polyatomic gas, the derivation is presented in [46], where besides the dynamical viscosity there also appears a second viscosity or bulk viscosity coefficient, which is equal to $(2/3)\tau pN/(N+3)$, where N represents the degrees of freedom in the molecule rotation and vibration.

For the 1D flow with only explicit U-velocity, the above viscous governing equations goes to

$$
\begin{pmatrix}\rho\\ \rho U\\ E\end{pmatrix}_t + \begin{pmatrix}\rho U\\ \rho U^2 + p\\ (E+p)U\end{pmatrix}_x = \begin{pmatrix}0\\ \frac{2K}{K+1}\tau pU_x\\ \frac{K+3}{4}\tau p\left(\frac{1}{\lambda}\right)_x + \frac{2K}{K+1}\tau pUU_x\end{pmatrix}_x,
$$

where in this case K is defined by $K = (3-\gamma)/(\gamma-1)$ and $E = \frac{1}{2}\rho(U^2 + \frac{K+1}{2\lambda})$. Notice that for the 1D flow the molecular motion in both the y- and the z-direction is included as internal variable, and the above expression K is different from the K defined previously for the 2D flow. For example, for a monatomic gas in 1D case K is equal to 2, which accounts for the molecular motion in the y and z-directions. In this case, the above Navier–Stokes equations go to the standard form,

$$
\begin{pmatrix}\rho\\ \rho U\\ E\end{pmatrix}_t + \begin{pmatrix}\rho U\\ \rho U^2 + p\\ (E+p)U\end{pmatrix}_x = \begin{pmatrix}0\\ \frac{4}{3}\mu U_x\\ \frac{5}{4}\mu\left(\frac{1}{\lambda}\right)_x + \frac{4}{3}\mu UU_x\end{pmatrix}_x,
$$

where $\mu = \tau p$ is the dynamical viscosity coefficient. With the relation $\lambda = m/2kT$ and $C_p = 5k/2m$ for a monatomic gas, the heat conduction coefficient in the above equations becomes $\kappa = 5k\mu/2m$, and the Prandtl number becomes fixed with the value $Pr = \mu C_p/\kappa = 1$. This is a well-known result for the BGK model. For the NS equations for a monatomic gas with arbitrary Prandtl number, the only change from the above equations is that the heat conduction coefficient is changed from $5k\mu/2m$ to $5k\mu/2m\,Pr$. In Appendix C, the Navier–Stokes equations with arbitrary Prandtl numbers and the viscosity law $\mu \sim T^{0.8}$ are solved for the shock structure solution.

This paper is targeting the numerical NS solutions. Both the initial gas distribution function and the equilibrium state in the BGK model are evaluated based on the *linear distribution* of macroscopic flow variables. Theoretically, the physical content in the BGK model is far richer than the Navier–Stokes equations, especially in the rarefied regime [22, 43].

2.3. *BGK Flow Solver*

The general solution f of the BGK model (2) at a cell interface $x_{j+1/2}$ and time t is

$$f\left(x_{j+1/2}, t, u, v, \xi\right) = \frac{1}{\tau}\int_0^t g(x', t', u, v, \xi)e^{-(t-t')/\tau}dt' + e^{-t/\tau}\, f_0\left(x_{j+1/2} - ut\right), \quad (6)$$

where $x' = x_{j+1/2} - u(t - t')$ is the particle trajectory and f_0 is the initial gas distribution function f at the beginning of each time step ($t = 0$). Two unknowns g and f_0 must be specified in Eq. (6) in order to obtain the solution f. In order to simplify the notation, $x_{j+1/2} = 0$ will be used in the following text.

In all previous BGK schemes [46], based on the initial macroscopic variables, see Fig. 2, the initial gas distribution function f_0 is assumed to be

$$f_0 = \begin{cases} g^l\left[1 + a^l x\right], & x \le 0, \\ g^r\left[1 + a^r x\right], & x \ge 0, \end{cases} \quad (7)$$

where g^l and g^r are the Maxwellian distributions at the left and right of a cell interface. The slopes a^l and a^r come from the spatial derivative of a Maxwellian and have a unique correspondence with the slopes of the conservative variables. Note that the formulation of a^l and a^r will be given later. The basic assumption in the above formula is that, even with a discontinuity at the cell interface, the gas is assumed to stay in an equilibrium state on both sides of the discontinuity. This assumption is valid for any flow simulation, where the cell size Δx cannot properly resolve the viscous flow structure, such as in the cases for the inviscid Euler equations. When the cell size is much larger than the shock thickness, the shock does appear as a discontinuity and the flows in the upstream and downstream stay in equilibrium states. However, if the mesh size becomes fine enough to well resolve the physical shock structure, the initial gas distribution function f_0 should give an accurate description of the real physical situation inside a shock layer, which deviates from an equilibrium Maxwellian. Therefore, a nonequilibrium state must be used in this case. In order to represent the general situation, in the current paper the initial gas distribution function f_0 is assumed to have the form,

$$f_0 = \begin{cases} g^l[1 + a^l x - \tau(a^l u + A^l)], & x \le 0 \\ g^r[1 + a^r x - \tau(a^r u + A^r)], & x \ge 0, \end{cases} \quad (8)$$

where the additional terms are the nonequilibrium states obtained from the Chapman–Enskog expansion of the BGK model. Again, the detail formulation of (a^l, A^l, a^r, A^r) will be given at a later time. Basically, the additional terms $-\tau(a^l u + A^l)g^l$ and $-\tau(a^r u + A^r)g^r$ account for the deviation of a distribution function away from a Maxwellian. In other words, the gas is out of equilibrium automatically by virtue of a spatial distribution of macroscopic quantities, such as the gradients of density, velocity, and temperature. Since the nonequilibrium parts have no direct contribution to the conservative variables, i.e.,

$$\begin{aligned} \int (a^l u + A^l)\psi g^l d\Xi = 0, \\ \int (a^r u + A^r)\psi g^r d\Xi = 0, \end{aligned} \quad (9)$$

both distributions in Eqs. (7) and (8) correspond to the same macroscopic variables shown in Fig. 2. Keeping an initial nonequilibrium state in the gas distribution gives a more realistic description of the flow motion in the dissipative region. Many kinetic schemes have used the Chapman–Enskog distribution function of the Boltzmann equation directly as the initial condition [8, 21].

After having f_0, the equilibrium state g around $(x = 0, t = 0)$ is assumed to have two slopes, which is different from the assumption in the previous NS BGK scheme [52],

$$g = g_0[1 + (1 - \mathrm{H}[x])\vec{a}^l x + \mathrm{H}[x]\vec{a}^r x + \bar{A}t], \tag{10}$$

where $\mathrm{H}[x]$ is the Heaviside function defined as

$$H[x] = \begin{cases} 0, & x < 0, \\ 1. & x \geq 0. \end{cases}$$

Here g_0 is a local Maxwellian distribution function located at $x = 0$. Even though g is continuous at $x = 0$, it has different slopes at $x < 0$ and $x > 0$; see Fig. 3. In both f_0 and g, a^l, A^l, a^r, A^r, $\vec{a}^l$, $\vec{a}^r$, and $\bar{A}$ are related to the derivatives of a Maxwellian in space and time.

The dependence of $a^l, a^r, \ldots, \bar{A}$ on the particle velocities can be obtained from a Taylor expansion of a Maxwellian and has the following form,

$$\begin{aligned} a^l &= a_1^l + a_2^l u + a_3^l v + a_4^l \frac{1}{2}(u^2 + v^2 + \xi^2) = a_\alpha^l \psi_\alpha, \\ A^l &= A_1^l + A_2^l u + A_3^l v + A_4^l \frac{1}{2}(u^2 + v^2 + \xi^2) = A_\alpha^l \psi_\alpha, \\ &\cdots \\ \bar{A} &= \bar{A}_1 + \bar{A}_2 u + \bar{A}_3 v + \bar{A}_4 \frac{1}{2}(u^2 + \xi^2) = \bar{A}_\alpha \psi_\alpha, \end{aligned}$$

where $\alpha = 1, 2, 3, 4$, and all coefficients $a_1^l, a_2^l, \ldots, \bar{A}_4$ are local constants.

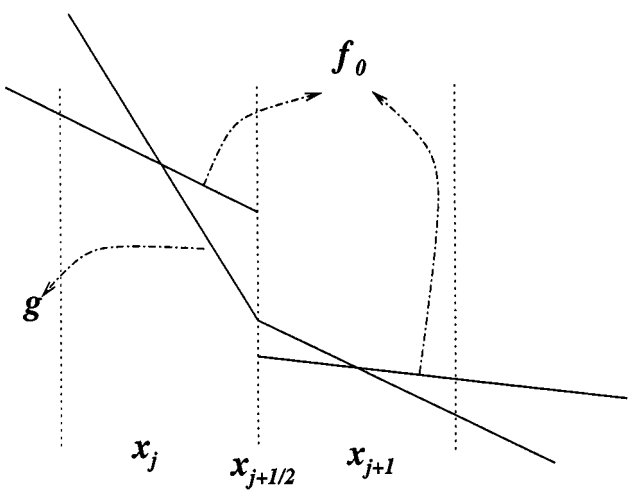

FIG. 3. The spatial distribution of the initial state f_0 and the equilibrium state g at $t = 0$. The evaluation of g from f_0 is given in Eqs. (15)–(17). The final gas distribution function f in Eq. (18) at the cell interface $x_{j+1/2}$ is a nonlinear combination of f_0 and g.

In the reconstruction stage described in the early section, we obtained the distributions $\bar{\rho}_j(x), \bar{m}_j(x), \bar{n}_j(x)$, and $\bar{E}_j(x)$ inside each cell $x_{j-1/2} \le x \le x_{j+1/2}$. At the cell interface $x_{j+1/2}$, the left and right macroscopic states are

$$\bar{w}_j\left(x_{j+1/2}\right) = \begin{pmatrix} \bar{\rho}_j\left(x_{j+1/2}\right) \\ \bar{m}_j\left(x_{j+1/2}\right) \\ \bar{n}_j\left(x_{j+1/2}\right) \\ \bar{E}_j\left(x_{j+1/2}\right) \end{pmatrix}, \quad \bar{w}_{j+1}\left(x_{j+1/2}\right) = \begin{pmatrix} \bar{\rho}_{j+1}\left(x_{j+1/2}\right) \\ \bar{m}_{j+1}\left(x_{j+1/2}\right) \\ \bar{n}_{j+1}\left(x_{j+1/2}\right) \\ \bar{E}_{j+1}\left(x_{j+1/2}\right) \end{pmatrix}.$$

By using the relation between the gas distribution function f and the macroscopic variables (Eq. 3), at $x_{j+1/2}$ we get

$$\int g^l \psi d\Xi = \bar{w}_j\left(x_{j+1/2}\right); \qquad \int g^l a^l \psi d\Xi = \frac{\bar{w}_j\left(x_{j+1/2}\right) - \bar{w}_j(x_j)}{\Delta x^-} \tag{11}$$

$$\int g^r \psi d\Xi = \bar{w}_{j+1}\left(x_{j+1/2}\right); \quad \int g^r a^r \psi d\Xi = \frac{\bar{w}_{j+1}(x_{j+1}) - \bar{w}_{j+1}\left(x_{j+1/2}\right)}{\Delta x^+}, \tag{12}$$

where $\Delta x^- = x_{j+1/2} - x_j$ and $\Delta x^+ = x_{j+1} - x_{j+1/2}$. With the definition of the Maxwellian distributions,

$$g^l = \rho^l \left(\frac{\lambda^l}{\pi}\right)^{\frac{K+2}{2}} e^{-\lambda^l((u-U^l)^2+(v-V^l)^2+\xi^2)},$$

$$g^r = \rho^r \left(\frac{\lambda^r}{\pi}\right)^{\frac{K+2}{2}} e^{-\lambda^r((u-U^r)^2+(v-V^r)^2+\xi^2)},$$

and from Eqs. (11) and (12), all the parameters in g^l and g^r can be uniquely determined,

$$\begin{pmatrix} \rho^l \\ U^l \\ V^l \\ \lambda^l \end{pmatrix} = \begin{pmatrix} \bar{\rho}_j\left(x_{j+1/2}\right) \\ \bar{m}_j\left(x_{j+1/2}\right)/\bar{\rho}_j\left(x_{j+1/2}\right) \\ \bar{n}_j\left(x_{j+1/2}\right)/\bar{\rho}_j\left(x_{j+1/2}\right) \\ \lambda^l \end{pmatrix}$$

and

$$\begin{pmatrix} \rho^r \\ U^r \\ V^r \\ \lambda^r \end{pmatrix} = \begin{pmatrix} \bar{\rho}_{j+1}\left(x_{j+1/2}\right) \\ \bar{m}_{j+1}\left(x_{j+1/2}\right)/\bar{\rho}_{j+1}\left(x_{j+1/2}\right) \\ \bar{n}_{j+1}\left(x_{j+1/2}\right)/\bar{\rho}_{j+1}\left(x_{j+1/2}\right) \\ \lambda^r \end{pmatrix},$$

where

$$\lambda^l = \frac{(K+2)\bar{\rho}_j\left(x_{j+1/2}\right)}{4\left(\bar{E}_j\left(x_{j+1/2}\right) - \frac{1}{2}\left(\bar{m}_j^2\left(x_{j+1/2}\right) + \bar{n}_j^2\left(x_{j+1/2}\right)\right)/\bar{\rho}_j\left(x_{j+1/2}\right)\right)}$$

and

$$\lambda^r = \frac{(K+2)\bar{\rho}_{j+1}(x_{j+1/2})}{4\big(\bar{E}_{j+1}(x_{j+1/2}) - \frac{1}{2}\big(\bar{m}^2_{j+1}(x_{j+1/2}) + \bar{n}^2_{j+1}(x_{j+1/2})\big)/\bar{\rho}_{j+1}(x_{j+1/2})\big)}.$$

Once g^r is obtained from the above equations, the slope a^r in Eq. (12) can be computed from

$$\frac{\bar{w}_{j+1}(x_{j+1}) - \bar{w}_{j+1}(x_{j+1/2})}{\rho^r \Delta x^+} = M^r_{\alpha\beta} \begin{pmatrix} a^r_1 \\ a^r_2 \\ a^r_3 \\ a^r_4 \end{pmatrix} = M^r_{\alpha\beta} a^r_\beta, \tag{13}$$

where

$$M^r_{\alpha\beta} = \int g^r \psi_\alpha \psi_\beta \, d\Xi/\rho^r.$$

The above matrix and the direct evaluation of the solution $(a^r_1, a^r_2, a^r_3, a^r_4)^T$ from the above equation are presented in Appendix B. For g^l, the matrix $M^l_{\alpha\beta} = \int g^l \psi_\alpha \psi_\beta d\Xi/\rho^l$ has the same structure as $M^r_{\alpha\beta}$, and $(a^l_1, a^l_2, a^l_3, a^l_4)^T$ in Eq. (11) can be obtained similarly. After having the terms a^l and a^r, A^l and A^r in f_0 can be found from Eq. (9), which are

$$\begin{aligned} M^l_{\alpha\beta} A^l_\beta &= -\frac{1}{\rho^l} \int g^l a^l u \psi_\alpha d\Xi, \\ M^r_{\alpha\beta} A^r_\beta &= -\frac{1}{\rho^r} \int g^r a^r u \psi_\alpha d\Xi. \end{aligned} \tag{14}$$

Since $M^l_{\alpha\beta}$, $M^r_{\alpha\beta}$, and the right-hand sides of the above equations are known, all parameters in A^l and A^r can be obtained subsequently using the method in Appendix B.

After determining f_0, the corresponding values of ρ_0, U_0, V_0, and λ_0 in g_0 of Eq. (10), i.e.,

$$g_0 = \rho_0 \left(\frac{\lambda_0}{\pi}\right)^{\frac{K+2}{2}} e^{-\lambda_0((u-U_0)^2+(v-V_0)^2+\xi^2)},$$

can be determined as follows. Taking the limit $t \to 0$ in Eq. (6) and substituting its solution into Eq. (4), the conservation constraint at $(x = x_{j+1/2},\ t = 0)$ gives

$$\int g_0 \psi \, d\Xi = w_0 = \int_{u>0} \int g^l \psi \, d\Xi + \int_{u<0} \int g^r \psi \, d\Xi, \tag{15}$$

where $w_0 = (\rho_0, m_0, n_0, E_0)^T$ is the macroscopic conservative flow variables located at the cell interface at time $t = 0$. This procedure in evaluating g_0 is different from the method used in [52]. Since g^l and g^r have been obtained earlier, the above moments can be evaluated explicitly. Therefore, the conservative variables ρ_0, m_0, n_0, and E_0 at the cell interface can be obtained, from which g_0 is uniquely determined. For example, λ_0 in g_0 can be found from

$$\lambda_0 = (K+2)\rho_0 \Big/ \left(4\left(E_0 - \frac{1}{2}\big(m_0^2 + n_0^2\big)/\rho_0\right)\right).$$

Then, $\bar{a}^l$ and $\bar{a}^r$ of g in Eq. (10) can be obtained through the relation of

$$\frac{\bar{w}_{j+1}(x_{j+1}) - w_0}{\rho_0 \Delta x^+} = \bar{M}^0_{\alpha\beta} \begin{pmatrix} \bar{a}^r_1 \\ \bar{a}^r_2 \\ \bar{a}^r_3 \\ \bar{a}^r_4 \end{pmatrix} = \bar{M}^0_{\alpha\beta} \bar{a}^r_\beta, \tag{16}$$

and

$$\frac{w_0 - \bar{w}_j(x_j)}{\rho_0 \Delta x^-} = \bar{M}^0_{\alpha\beta} \begin{pmatrix} \bar{a}^l_1 \\ \bar{a}^l_2 \\ \bar{a}^l_3 \\ \bar{a}^l_4 \end{pmatrix} = \bar{M}^0_{\alpha\beta} \bar{a}^l_\beta, \tag{17}$$

where the matrix $\bar{M}^0_{\alpha\beta} = \int g_0 \psi_\alpha \psi_\beta d\Xi/\rho_0$ is known; see Fig. 3 again. Therefore, $(\bar{a}^r_1, \bar{a}^r_2, \bar{a}^r_3, \bar{a}^r_4)^T$ and $(\bar{a}^l_1, \bar{a}^l_2, \bar{a}^l_3, \bar{a}^l_4)^T$ can be found following the procedure in Appendix B.

Up to this point, we have determined all parameters in the initial gas distribution function f_0 and the equilibrium state g at the beginning of each time step $t = 0$. After substituting Eqs. (8) and (10) into Eq. (6), the gas distribution function f at a cell interface can be expressed as

$$\begin{aligned} f\left(x_{j+1/2}, t, u, v, \xi\right) = & \left(1 - e^{-t/\tau}\right) g_0 \\ & + \left(\tau\left(-1 + e^{-t/\tau}\right) + t e^{-t/\tau}\right)(\bar{a}^l \mathrm{H}[u] + \bar{a}^r(1 - \mathrm{H}[u]))u g_0 \\ & + \tau\left(t/\tau - 1 + e^{-t/\tau}\right)\bar{A} g_0 + e^{-t/\tau}((1 - u(t+\tau)a^l)\mathrm{H}[u] g^l \\ & + (1 - u(t+\tau)a^r)(1 - \mathrm{H}[u]) g^r) + e^{-t/\tau}(-\tau A^l \mathrm{H}[u] g^l \\ & - \tau A^r (1 - \mathrm{H}[u]) g^r). \end{aligned} \tag{18}$$

The only unknown left in the above expression is $\bar{A}$. Since both f (Eq. (18)) and g (Eq. (10)) contain $\bar{A}$, the integration of the conservation constraint Eq. (4) at $x_{j+1/2}$ over the whole time step Δt gives

$$\int_0^{\Delta t} \int (g - f)\psi dt d\Xi = 0,$$

which goes to

$$\begin{aligned} \bar{M}^0_{\alpha\beta} \bar{A}_\beta \equiv & \frac{1}{\rho_0}(\partial\rho/\partial t, \partial m/\partial t, \partial n/\partial t, \partial E/\partial t)^T \\ = & \frac{1}{\rho_0} \int \left[\gamma_1 g_0 + \gamma_2 u(\bar{a}^l \mathrm{H}[u] + \bar{a}^r(1 - \mathrm{H}[u]))g_0 + \gamma_3(\mathrm{H}[u] g^l + (1 - \mathrm{H}[u]) g^r)\right. \\ & + \gamma_4 u(a^l \mathrm{H}[u] g^l + a^r(1 - \mathrm{H}[u]) g^r) + \gamma_5((a^l u + A^l)\mathrm{H}[u] g^l \\ & \left. + (a^r u + A^r)(1 - \mathrm{H}[u]) g^r)\right] \psi_\alpha d\Xi, \end{aligned} \tag{19}$$

where

$$\begin{aligned} \gamma_0 &= \Delta t - \tau\left(1 - e^{-\Delta t/\tau}\right), \\ \gamma_1 &= -\left(1 - e^{-\Delta t/\tau}\right)/\gamma_0, \\ \gamma_2 &= \left(-\Delta t + 2\tau\left(1 - e^{-\Delta t/\tau}\right) - \Delta t e^{-\Delta t/\tau}\right)/\gamma_0, \end{aligned}$$

$$\gamma_3 = \left(1 - e^{-\Delta t/\tau}\right)/\gamma_0,$$
$$\gamma_4 = \left(\Delta t e^{-\Delta t/\tau} - \tau\left(1 - e^{-\Delta t/\tau}\right)\right)/\gamma_0,$$
$$\gamma_5 = \tau\left(1 - e^{-\Delta t/\tau}\right)/\gamma_0.$$

Since all moments of the Maxwellian on the right-hand side of Eq. (19) can be evaluated using Appendix A, Eq. (19) can be solved to find $(\bar{A}_1, \bar{A}_2, \bar{A}_3, \bar{A}_4)^T$ using Appendix B again.

Finally, the time-dependent numerical fluxes in the x-direction across the cell interface can be computed as

$$\begin{pmatrix} \mathcal{F}_\rho \\ \mathcal{F}_m \\ \mathcal{F}_n \\ \mathcal{F}_E \end{pmatrix}_{j+1/2} = \int u \begin{pmatrix} 1 \\ u \\ v \\ \frac{1}{2}(u^2 + v^2 + \xi^2) \end{pmatrix} f\left(x_{j+1/2}, t, u, v, \xi\right) d\Xi, \tag{20}$$

where $f(x_{j+1/2}, t, u, v, \xi)$ is given in Eq. (18). By integrating the above equation to the whole time step, we can get the total mass, momentum, and energy transport. The above procedure can be repeated in the next time level.

In terms of computational efficiency, as a result of the moments evaluation and error function in the gas-kinetic scheme, the BGK scheme is slower than the central difference and most upwinding schemes. As pointed out in [5], for the 2D viscous flow calculations, the BGK-type schemes are approximately two times slower than the Roe-type scheme for the NS equations. The KFVS NS solver, which is a simplification of the BGK scheme discussed in the next section, should have the similar speed as Godunov-type NS solver.

2.4. *Analysis*

In this section, we will analyze the BGK scheme presented in the last section. Many issues related to the kinetic limits, collision time, Prandtl number fix, and boundary condition will be addressed.

2.4.1. Gas-kinetic Navier–Stokes solver. In order to verify that Eq. (18) gives a correct Navier–Stokes solution, let's consider the following limiting case. Equation (18) gives explicitly the time-dependent gas distribution function f at the cell interface. In a well-resolved flow region, such as inside a resolved shock layer, the reconstructed conservative variables in Fig. 2 will become approximately a straight line. In such a case, the distribution function f_0 has $g^l = g^r$ and $a^l = a^r$. Consequently, Eq. (15) gives $g_0 = g^l = g^r$, and Eqs. (16) and (17) reduce to $\bar{a}^l = \bar{a}^r = a^l = a^r$. As a result, $\bar{A}$ determined in Eq. (19) is exactly equal to A^l and A^r in Eq. (14). Therefore, without any further assumption, the gas distribution function f at a cell interface becomes

$$f = g_0[1 - \tau(u\bar{a} + \bar{A}) + t\bar{A}], \tag{21}$$

where $-\tau(u\bar{a} + \bar{A})g_0$ is exactly the nonequilibrium state from the Chapman–Enskog expansion of the BGK model [46], and $g_0\bar{A}t$ is the time evolution part of the gas distribution function. The above equation (21) is the one we used for the low Mach number viscous flow calculations [37], where the accuracy of the above formulation is well established.

But, similar to many other compressible codes extended to the low-speed flow calculation, stiffness problems will appear when the kinetic energy of flow is much less than the thermal one, and the time step determined by the Courant–Friedrichs–Levy (CFL) condition becomes very small because of the large sound speed. Note that in deriving Eq. (21), we have not required the assumption $\tau < \Delta t$, which has been used previously [46]. The only requirement here is that the dissipative region is well resolved. However, when resolving a dissipative region with a few grid points, such as 5–10 grid points in the boundary layer, a small jump in the initial reconstructed data at a cell interface will probably appear. Even with the discontinuities at a cell interface, because of the formation of an equilibrium state in the BGK scheme, Eq. (21) is still the main contribution in the gas distribution function f (18) in the case of $\tau < \Delta t$. But, for the KFVS scheme based on the collisionless Boltzmann equation, once there is a discontinuous jump at a cell interface, the gas evolution is dominant by the free transport from the initial term f_0, where the intrinsic dissipative coefficient will be proportional to the time step. In the case $\tau \gg \Delta t$, as analyzed later, the physical viscosity coefficient becomes dominant, and both the BGK and the KFVS schemes give an accurate NS solution.

In the paper by Chae, Kim, and Rho [5], they basically interpolated $g_0 u\bar{a}$ as the nonequilibrium state of the Chapman–Enskog expansion of the BGK model. Actually, the correct form should be $g_0(u\bar{a} + \bar{A})$, and only this one could satisfy the requirement $\int g_0(\bar{a}u + \bar{A})\psi d\Xi = 0$.

2.4.2. Collision time. In a resolved dissipative region, such as the cell size, Δx is much smaller than the dissipative length scale determined by the physical viscosity, the collision time τ in the BGK scheme can be naturally determined by the relation

$$\tau = \mu / p,$$

where μ is the dynamical viscosity coefficient and p is the pressure. Since the BGK model gives a fixed Prandtl number $\Pr = 1.0$, only one coefficient can be set correctly in the viscous flow simulation, i.e., the viscosity or heat conduction. A numerical fix, or more precisely a new discretized physical model, to make both coefficients correct will be addressed next in the Prandtl number fix section. For the viscosity coefficient, μ can take any reasonable form in the determination of τ. The simplest case is that μ keeps a constant. In the shock-boundary interaction case, μ will take the Sutherland's law,

$$\mu = \mu_\infty \left(\frac{T}{T_\infty} \right)^{3/2} \frac{T_\infty + S}{T + S},$$

where T_∞ and S are the temperatures with the values $T_\infty = 285\ K$ and $S = 110.4\ K$. In the shock structure calculation, $\mu \propto T^\omega$ is also used. The local collision time in the BGK scheme is determined in the following. From the constructed macroscopic variables at a cell interface, such as w_0 in Eq. (15), we can evaluate $\mu(w_0)$ according to the above formulation, where T is the temperature evaluated from w_0. Then, the local collision time τ is defined with the value $\tau = \mu(w_0)/p$, where p is the pressure and is a function of w_0 also.

Theoretically, the dissipative structure, such as the shock thickness, is solely determined by the physical viscosity. The structure should be independent of the cell size and time step used in a numerical scheme. However, even if the Navier–Stokes equations are precisely solved, when the cell size is not fine enough to resolve the wave structure, the physical

structure has to be replaced by a numerical one. For example, the physical shock thickness may be replaced by the numerical cell size. In such a situation, we cannot solve the Navier–Stokes equations with the original physical viscosity. The effective viscosity should be a combination of both the physical and numerical ones. Different from many upwinding schemes, the BGK method cannot simply take an apology to admit that the implicit numerical dissipation is included in the under-resolved flow region. Since the BGK method is an accurate Navier–Stokes flow solver, even in the under-resolved discontinuity region, the additional numerical viscosity is required to have a numerical shock thickness on the order of cell size. Since the jump at the cell interface (see Fig. 2), indicates basically the under-resolveness of the flow structure, the collision time τ used in all simulations in this paper takes into account the pressure jump and has the form

$$\tau = \frac{\mu(w_0)}{p(w_0)} + \frac{|\rho_l/\lambda_l - \rho_r/\lambda_r|}{|\rho_l/\lambda_l + \rho_r/\lambda_r|}\Delta t, \tag{22}$$

where Δt is the CFL time step. The second part corresponds to the numerical viscosity. This construction of dissipation is based on the similar consideration as the Jameson–Schmidt–Turkel (JST) scheme [20]. In the smooth flow region or around the slip line, the artificial dissipation introduced above is very small or diminishes because of the continuous pressure distribution. As shown in the test cases, the enhancement of the particle collision time does not deteriorate the boundary or shock layer calculations, but increases the robustness of the BGK scheme.

The obvious advantage of the BGK method is that it solves a viscous governing equation with an explicit dissipative term, which avoids the ambiguity of implicit dissipation in many upwinding schemes [39]. Even though the shock jump with a width of 2 or 3 cell size can be captured nicely in the Godunov-type schemes, the dissipation there for the construction of such a shock structure is solely coming from the numerics. There is no reason to guarantee that the purely numerical and implicit dissipative mechanism could always be consistent with the physical one [49]. The BGK scheme explicitly includes the physical and numerical mechanisms into a single algorithm. The fluid behavior in both smooth and discontinuous regions is treated uniformly by the collisional BGK model with an adaptation of local particle collision time.

2.4.3. Limiting cases. The BGK scheme is designed to have a valid Navier–Stokes solution in both $\tau < \Delta t$ and $\tau > \Delta t$ regions. If the collision time τ is much larger than the time step Δt, i.e., $\tau \gg \Delta t$, the BGK model goes to the collisionless Boltzmann equation, $f_t + u f_x = 0$, and the gas distribution function (18) in this case goes to

$$\begin{aligned} f &= f_0(x - ut) \\ &= [1 - \tau(ua^l + A^l) - tua^l]\,\mathrm{H}[u]g^l + [1 - \tau(ua^r + A^r) - tua^r](1 - \mathrm{H}[u])g^r. \end{aligned} \tag{23}$$

This is a second-order time accurate scheme for the collisionless Boltzmann equation. If the above distribution function is further simplified, such as deleting the time dependent part, a constant flux function can be obtained from the above distribution function,

$$f = [1 - \tau(ua^l + A^l)]\,\mathrm{H}[u]g^l + [1 - \tau(ua^r + A^r)](1 - \mathrm{H}[u])g^r. \tag{24}$$

The above distribution is basically the KFVS NS scheme developed by Chou and Baganoff [8]. In their approach, a direct implementation of the Chapman–Enskog expansion of the

Boltzmann equation is used to split the fluxes. The nonequilibrium state in our case is solely consistent with the BGK model. From the BGK scheme, we can clearly understand the limitation of the Chou–Baganoff's KFVS NS method. Because Eq. (24) is the limiting case of Eq. (18) with $\tau \gg \Delta t$, Eq. (24) is only valid for the Navier–Stokes solution under such a limiting condition. In other words, the KFVS NS scheme approaches the Navier–Stokes solution accurately if the condition $\mu/p \gg \Delta t$ is satisfied. In $\mu/p < \Delta t$ region, the KFVS NS scheme may behave differently from the Navier–Stokes solution. Inherently, the transport formulation in Eq. (24) uses the time step Δt as the particle collision time, which could be much larger than the physical collision time τ. This artifact can be ignored only under the condition $\Delta t \ll \tau = \mu/p$, where the physical viscous term plays a dominant role. In order to get a clear understanding about the above analysis, let us see some examples. In the following analysis, we are going to qualitatively estimate the KFVS NS scheme in the shock and boundary layer applications. Because of the free transport mechanism in the KFVS scheme, the numerical viscous coefficient becomes $\mu_{num} \simeq p\Delta t$, where p is the pressure and Δt is the time step. Since the time step is determined by the CFL condition, the artificial dissipation can also be written as $\mu_{num} \sim (\rho/(\gamma(1+M)))c\Delta x \sim \rho c \Delta x$, where Δx is the cell size, c is the sound speed, and M is the Mach number. Suppose we need $N \simeq 10$ cells to resolve a NS shock structure or a boundary layer. Since the shock thickness is proportional to the mean free path l_s, in the resolved shock region the mesh size must satisfy $\Delta x = l_s/N$. Then, in the stationary shock case, because of the conditions $M \geq 1$ and $Re \simeq 1$, we have

$$\frac{\mu_{num}}{\mu_{phys}} \simeq \frac{c\Delta x\, Re}{l_s U} \simeq \frac{Re}{M}\left(\frac{\Delta x}{l_s}\right) \simeq \frac{Re}{M}\left(\frac{1}{N}\right) \ll 1.$$

Therefore, the KFVS NS scheme could give an accurate NS shock structure once the shock structure is resolved. This has been numerically proven in [8]. However, if the boundary layer is resolved with the same number of grid points, such as $l_b = N\Delta x$, we have

$$\frac{\mu_{num}}{\mu_{phys}} \simeq \frac{c\Delta x\, Re}{LU} \simeq \frac{Re}{M}\left(\frac{\Delta x}{L}\right) \simeq \frac{\sqrt{Re}}{M}\left(\frac{1}{N}\right),$$

where L is the length of the flat plate. The boundary layer thickness $l_b \simeq \sqrt{\nu L/U}$ has been used in the above approximation. Therefore, for a subsonic boundary layer with $M < 1$ and $Re \gg 1$, i.e., $M = 0.3$ and $Re = 10^5$, the numerical dissipation could dominant the physical one $\mu_{num} \gg \mu_{phys}$ when the grid point in the boundary layer is on the order of $N = 10$. So, the KFVS NS scheme cannot be properly used in this case. The KFVS NS scheme is tested in the boundary layer case in Fig. 22, where Eq. (23) and (24) are used.

Mathematically, it is true that in the continuum limit Eq. (24) will go to Eq. (21) also at time $t = 0$, which is the Chapman–Enskog expansion of the BGK model. But, how could it have different behavior numerically? The reason for this is that the mathematical assumption could not be satisfied numerically in the boundary layer case, when a limited number of grid points and a second-order interpolation rule are used. For example, with the implementation of the van Leer limiter, the interpolated left and right states and their slopes can hardly be exactly equal to each other inside the boundary layer. If the difference between g^l and g^r appears, the BGK scheme and the KFVS NS method behave differently. For the BGK scheme, in the $\tau < \Delta t$ case the particles from the left and right states will suffer particle collisions to form an equilibrium state there, which prevents the free particle

penetration, and Eq. (21) is the dominant part in the gas distribution function (18) for the flux evaluation. However, the particles in the KFVS NS solver could go freely to the neighboring cells, and each particle has the mean free path on the order of the cell size. As shown in Eq. (24), because of the lack of particle collisions, the individual g^l and g^r contribute solely to the flux, and there is no any tendency for them to form an equilibrium state. So, it is not surprising that for the viscous flow calculations many high-resolution schemes are very sensitive to the interpolation techniques used [10], and that an interpolation higher than second-order is basically required. They need to reduce the difference in the interpolated left and right states as much as possible in order to reduce the free transport mechanism. Otherwise, the difference in the initial states will trigger the dynamical deficiency and distort the physical picture. But, this kind of fix, using interpolation to conceal the gas evolution problem, is only an *ad hoc* fix. Difficulties will be appear in the cases when the high-order interpolation rule cannot work properly, such as in the case with limited grid points in the boundary layer and the cases with unstructured mesh. On the other hand, the scheme based on the collisional BGK model does not have such a sensitivity to the interpolation because of the implementation of the particle collisional mechanism. Notice that the dissipative mechanism in the Flux Difference Splitting (FDS) methods, such as the Godunov and Roe's methods, is different from that in the FVS schemes because of the wave interactions from the left and right states [49].

For the Euler solution, Eq. (24) can be further simplified,

$$f = \mathrm{H}[u]g^l + (1 - \mathrm{H}[u])g^r, \tag{25}$$

where the nonequilibrium state is totally removed. This is precisely the EFM or KFVS scheme for the compressible Euler equations [27, 30, 32, 33]. The above KFVS scheme has been well studied and applied to many physical and engineering problems. Recently, in order to prove the entropy condition for the first-order KFVS scheme, a new concept of distinguishable particles in different numerical cells has been introduced [25]. An earlier version of the above KFVS scheme is the beam scheme, where instead of using Maxwellians, the equilibrium states g^l and g^r are replaced by three Delta functions or particles [35]. As analyzed recently [38], the Steger–Warming method can be represented as a "beam scheme" also. However, because of their slight difference in the particle representation, such as the lack of internal energy in the second "particle" in the Steger–Warming method [38], it could be less robust than the beam scheme. The relation between the beam scheme and the Lattice Boltzmann method is analyzed in [50].

With the above connection between the KFVS scheme and the Steger–Warming method, it is easy to understand the poor performance of many FVS schemes in the viscous boundary layer calculations [36, 41, 42]. Similar to the KFVS scheme, these FVS NS solvers are valid under the condition $\mu/p \gg \Delta t$. Because of the symmetric lattice and diagonal transport mechanism, the Lattice Boltzmann Method (LBM) is very fortunate in this aspect. It does present an accurate NS solution in the incompressible limit [7, 16]. Because, with a symmetric lattice, the free particle transport process introduces an artificial viscous term which is consistent with the NS viscous term in the low speed limit and the viscosity coefficient is proportional to $-\frac{1}{2}\Delta t$. Therefore, with a fixed time step the numerical dissipative term can be absorbed in the physical one [21]. As a result, the final viscosity coefficient in the Lattice BGK (LBGK) method is proportional to $(\tau - \Delta t/2)\,p$, where $\Delta t = 1$ is usually used. There is not a precise analogue between the finite volume KFVS scheme and the Lattice

Boltzmann method. Because of cell averaging, reconstruction process, and the nonisotropic transport, such as the lack of diagonal particle or wave motion, the KFVS scheme has a much more complicated dissipative nature. But, the numerical viscosity coefficient μ_{num} can be still approximately estimated for the KFVS scheme using a simple shear flow model [26], which gives the same result as $\tau = \Delta t$ in the LBGK method, such that $\mu_{num} \sim p\Delta t/2$. The LBGK method tells us that the development of a multidimensional scheme will depend severely on the mesh construction. More precisely, it depends on whether a numerical mesh could preserve the isotropic and homogeneous properties of the real fluid equations. For the Lattice Boltzmann methods, the symmetry, invariants, and so forth, are the main concerns in their algorithm developments.

2.4.4. Prandtl number fix. It is well known that the BGK scheme corresponds to unit Prandtl number. In order to change the above Prandtl number to any realistic value, many attempts have been proposed. The most well-known is probably the BGK-Ellipsoidal-Statistical (BGK-ES) collision operator [18], in which the equilibrium state in the BGK model is replaced by an anisotropic Gaussian (without considering internal variables),

$$G = \frac{\rho}{\sqrt{\det(2\pi\mathcal{T})}} \exp\left(-\frac{1}{2}(u_i - U_i)\mathcal{T}^{-1}(u_j - U_j)\right),$$

where $\rho\mathcal{T} = \frac{1}{Pr} RTI + (1 + \frac{1}{Pr})\rho\Phi$ is a linear combination of the stress tensor $\rho\Phi = \int (u_i - U_i)(u_j - U_j) f d\Xi$ and of the Maxwellian isotropic stress tensor ρRTI. If we extend the current BGK scheme to the above BGK-ES model, considerable work has to be devoted to capture the time evolution of the above anisotropic stress tensor.

As mentioned earlier, the BGK model itself can always make one coefficient correct, e.g., the viscosity or heat conduction. In the BGK method, we obtained explicitly the time-dependent gas distribution function f at the cell interface Eq. (18). Therefore, the time-dependent heat flux can be evaluated precisely,

$$q = \frac{1}{2}\int (u - U)((u - U)^2 + (v - V)^2 + \xi^2) f d\Xi, \tag{26}$$

where the average velocities U and V are defined by

$$U = \int u f d\Xi \Big/ \int f d\Xi, \quad V = \int v f d\Xi \Big/ \int f d\Xi.$$

Then, the easiest way to fix the Prandtl number for the BGK scheme is to modify the energy flux by subtracting the above heat flux (26) and adding another one with a variable Prandtl number,

$$\mathcal{F}_E^{new} = \mathcal{F}_E + \left(\frac{1}{\mathrm{Pr}} - 1\right) q, \tag{27}$$

where $\mathcal{F}_E$ is the energy flux in Eq. (20).

In a smooth flow region, the above Prandtl number fix can be further simplified. Since the gas distribution function in such a case reduces to $f = g_0[1 - \tau(\bar{a}u + \bar{A}) + t\bar{A}]$, the

corresponding heat flux is

$$
\begin{aligned}
q_s &= -\tau \int g_0(u-U_0)\left(\psi_4 - U_0\psi_2 - V_0\psi_3 + \frac{1}{2}\left(U_0^2+V_0^2\right)\right)(\bar{a}u+\bar{A})\,d\Xi \\
&= -\tau \int g_0(u-U_0)(\psi_4 - U_0\psi_2 - V_0\psi_3)(\bar{a}u+\bar{A})\,d\Xi \\
&= -\tau \int g_0(\bar{a}u^2\psi_4 + \bar{A}u\psi_4 - U_0(\bar{a}u^3+\bar{A}u^2) - V_0(\bar{a}u^2v+\bar{A}uv))\,d\Xi. \qquad (28)
\end{aligned}
$$

Therefore, in this case we can simply replace q in Eq. (27) by the above q_s. This is the formula we use in the Couette flow, in shock structure, and in shock boundary interaction cases in the next section, where excellent results have been obtained in all cases from near-equilibrium to highly nonequilibrium. There will not be much CPU time involved in the above Prandtl number fix, since all momentum in Eq. (28) has been obtained already in the evaluation of the original energy flux $\mathcal{F}_E$. The above Prandtl number fix with the evaluation of q_s is based on the similar consideration as the method proposed in [5]. The difference is that all terms related to $\bar{A}$ in Eq. (28) was ignored in [5], which does not correspond to the Chapman–Enskog expansion. For the KFVS scheme, since there is not a collisional model and a corresponding Chapman–Enskog expansion, a variable Prandtl number can be implemented directly in the initial gas distribution function.

The Prandtl number fix (27) is more like a physical model in the discretized level. It is applied every time step when evaluating the fluxes (20) at the cell interface. To the Navier–Stokes order, the above fix seems physically reasonable. Theoretically, the BGK-ES model is also a numerical fix, but it is on the dynamical level. Dynamically, keeping an anisotropic Gaussian for the equilibrium distribution function seems to have no direct physical basis even through it could make the Prandtl number correct in the Chapman–Enskog order. The real physical weakness of the BGK model is that the collision time is independent of particle velocity, this fact is different from the phenomena with an anisotropic temperature distribution, where the temperature is directionaly dependent.

Any numerical scheme is more or less like a discretized gas evolution model. The BGK scheme with the Prandtl number fix can be considered as a new kinetic model on the numerical level. We are usually accustomed to the idea of using the analytical physical model to judge the discretized model. However, if we consider the flow problems on the discretized space directly, we may have a different opinion. If we want to evaluate different schemes, the most important thing is to make our discretized model to describe the physical reality (not necessarily to be the equations) as truthfully as possible, such as the process of constructing of the physical model in the derivation of the governing equation. Sometimes, a successful numerical scheme, such as the DSMC method [2], is based on the physical model of the particle transport and collisions, rather than any well-defined governing equation. In some cases, such as the multicomponent nonequilibrium chemical reactive flow, we do not even have a faithful governing equation yet, but we can still simulate it through the discretized particle interaction model. So, for the algorithm development, we should care more about the underlying physical model of the discretized scheme, rather than the equations to be discretized. Even based on the same inviscid Euler equations, the exact or approximate Riemann solvers have different interpretation of the flow evolution. For example, the FVS scheme actually solves a viscous governing equation even though it is a discretization of the inviscid one.

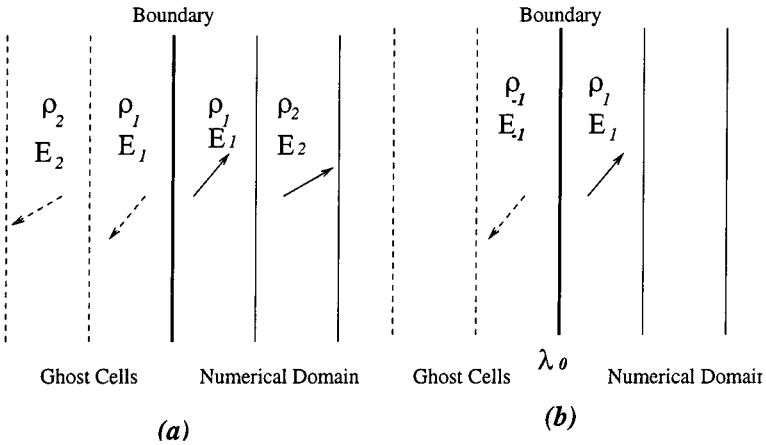

FIG. 4. Boundary condition. (a) adiabatic boundary condition, where the mass and energy densities are distributed symmetrically around the boundary and the velocities are reversed. (b) isothermal boundary condition, where the velocity vector is reversed in the ghost cell, but the mass and energy densities are given by Eqs. (29) and (30).

2.4.5. Boundary condition. The molecular interaction of the gas flow with the solid boundary in different flow situations has been explicitly pointed out by Patterson [29]. This subsection is mainly about how to implement these ideas numerically in the gas-kinetic BGK scheme.

For the Navier–Stokes equations, the no-slip boundary condition is obtained by creating two ghost cells, where the velocities in the ghost cells are reversed from the velocities inside the computational domain; see Fig. 4. For the adiabatic wall condition, where there is no heat flow through the boundary, the mass and energy densities in the ghost cells should be symmetric around the boundary,

$$\rho_{-1} = \rho_1, \quad E_{-1} = E_1,$$
$$\rho_{-2} = \rho_2, \quad E_{-2} = E_2,$$

where -1 and -2 represent the first and second ghost cells. Because of the above boundary condition, we can easily prove that the mass flux $\mathcal{F}_\rho = 0$ and the heat flux $q = 0$ at the wall for the BGK scheme.

For the isothermal boundary condition, where the boundary keeps a fixed temperature, such as $\lambda_0 = m/(2kT_0)$, in order to keep a second-order accuracy of the scheme at the boundary we have to carefully derive the flow variables in the ghost cell. In the following, we only consider the case where the nonlinear limiter is not applied at the boundary cells. Therefore, we only need to construct the flow variables in the first ghost cell, see Fig. 4. In order to have the non-slip condition, we first have

$$U_{-1} = -U_1, \quad V_{-1} = -V_1,$$

which gives $U_0 = 0$ and $V_0 = 0$ at the wall. Since the temperature at $x = 0$ (location of the boundary) has a fixed value λ_0, the slope of temperature in space at the boundary is

$$\left(\frac{\partial \lambda}{\partial x}\right)_0 = \frac{\lambda_1 - \lambda_0}{\frac{1}{2}\Delta x},$$

where λ_1 is the "temperature" of the cell averaged flow variables in the first cell inside the computation domain. Therefore, the temperature in cell –1 becomes

$$\lambda_{-1} = \lambda_0 - \frac{1}{2}\Delta x\left(\frac{\partial \lambda}{\partial x}\right)_0.$$

Since the energy density in cell –1 is determined by

$$E_{-1} = \frac{1}{2}\rho_{-1}\left(U_{-1}^2 + V_{-1}^2\right) + \frac{1}{\gamma - 1}\frac{\rho_{-1}}{2\lambda_{-1}}, \tag{29}$$

the only unknown in the above formulation is ρ_{-1}. In order to determine ρ_{-1}, we need to use the condition that there is no net mass flux transport across the boundary. Since the mass transport in a time step Δt can be expressed as (no limiter involved),

$$\begin{aligned}
\Delta m = 0 &= \int_0^{\Delta t}\int u[1 - \tau(\bar{a}u + \bar{A}) + t\bar{A}]\, g_0 dt d\Xi \\
&= \int_0^{\Delta t}\int u(1 + t\bar{A}) g_0 dt d\Xi \\
&= \Delta t(\rho_0 U_0) - \frac{1}{2}(\Delta t)^2 \int \bar{a}u^2 g_0 d\Xi \\
&= -\frac{1}{2}(\Delta t)^2\left(\frac{1}{2\lambda_0}\left(\frac{\partial \rho}{\partial x}\right)_0 - \frac{\rho_0}{2\lambda_0^2}\left(\frac{\partial \lambda}{\partial x}\right)_0\right),
\end{aligned}$$

which gives

$$\frac{1}{\rho_0}\left(\frac{\partial \rho}{\partial x}\right)_0 = \frac{1}{\lambda_0}\left(\frac{\partial \lambda}{\partial x}\right)_0.$$

The discretized form of the above equation is

$$\frac{\rho_1 - \rho_{-1}}{\rho_1 + \rho_{-1}} = \frac{1}{2\lambda_0}\left(\frac{\partial \lambda}{\partial x}\right)_0 \Delta x, \tag{30}$$

from which ρ_{-1} can be derived. The above isothermal boundary condition will be used in the Couette flow simulation. For a moving isothermal boundary with a velocity V_0 in the perpendicular direction, the only change from the above isothermal boundary condition is that V-velocity in the first ghost cell –1 is replaced by

$$V_{-1} = V_0 - \frac{1}{2}\Delta x\left(\frac{\partial V}{\partial x}\right)_0,$$

where $(\partial V/\partial x)_0 = 2(V_1 - V_0)/\Delta x$.

Another important observation from the kinetic scheme is that it can introduce a slip condition easily through the use of an appropriate flux boundary condition. The kinetic scheme can be matched with the DSMC method in the near continuum regime only after the implementation of the slip condition at the solid boundaries. The basic formulation of kinetic slip boundary is based on the fact that with the introduction of gas distribution function, we can explicitly evaluate the amount of particles hitting the boundary. Then according to the

accommodation coefficients for the momentum and energy, and the temperature at the wall, we can re-emit the same amount of particles with a predescribed distribution function. As a result, the appearance of slip at the boundary is obtained naturally and is consistent with the DSMC type boundary condition in the near continuum regime because of their common kinetic considerations. More discussion and the specific application of the slip boundary can be found in many kinetic books and papers [2, 4, 8, 22, 29].

3. NUMERICAL EXPERIMENTS

The current scheme has been applied to several test cases ranging from simple Couette flow to the complicated shock-boundary interaction. Unless otherwise stated, in all numerical examples reported here, the particle collision time is given by Eq. (22) and $\gamma = 1.4$. The time step Δt in all calculations are determined by CFL condition. All steady state solutions are obtained from the time accurate BGK solver with a long-time integration. Except specifically mentioned, the initial slopes for the conservative variables are obtained using the van Leer limiter.

Case 1. *Couette Flow with a Temperature Gradient*

Couette flow with a temperature gradient provides a good test for the BGK scheme to describe the viscous heat conducting flow. With the bottom wall fixed, the top boundary is moving at a speed U in the horizontal direction. The temperatures at the bottom and top are fixed with values T_0 and T_1. Under the assumption of constant viscosity and heat conduction coefficients and in the incompressible limit, a steady state analytic temperature distribution can be obtained,

$$\frac{T - T_0}{T_1 - T_0} = \frac{y}{H} + \frac{\mathrm{PrEc}}{2}\frac{y}{H}\left(1 - \frac{y}{H}\right), \tag{31}$$

where H is the height of the channel, Pr is the Prandtl number, Ec is the Eckert number $\mathrm{Ec} = U^2/C_p(T_1 - T_0)$, and C_p is the specific heat ratio at constant pressure.

We set up the simulation as a 1D problem in the x-direction. There are 20 grid points used in this direction from 0 to 1 with $H = 1.0$. The moving velocity at the right boundary in the y-direction is $V_1 = 1.0$. The initial density and Mach number of the gas inside the channel are 1.0 and 0.1, respectively. So, the fluid in the channel is almost incompressible. The isothermal no-slip boundary conditions are implemented at both ends. We have tested the current BGK scheme with a wide range of parameters: (i) specific heat ratio $\gamma = 7/5, 5/3$, and 2.0, (ii) different Prandtl number $\mathrm{Pr} = 0.5$, 0.72, 1.0, 1.5, and 2.0, and (iii) different collision time τ, which ranges from $0.01\Delta t$ to $1.5\Delta t$. With the variations of all these parameters, the simulation results fit the exact solutions very well. Figures 5 and 6 present the solutions in a few cases with different Prandtl numbers and Eckert numbers. From these figures, we see that the Prandtl number fix does modify the heat conduction term correctly.

In the above case, the velocity in the channel is linearly distributed. For a highly dissipative flow, an analytic expression in terms of y/H is not available. In the following, we are going to test the BGK scheme when the stress and heat flux are large. When the velocity of the upper wall is large enough, the compressibility of the fluid becomes appreciable. Under the conditions of $\mu \sim T^\omega$ with $\omega = 1$ and of adiabatic lower wall condition $q_w = 0$, there is an

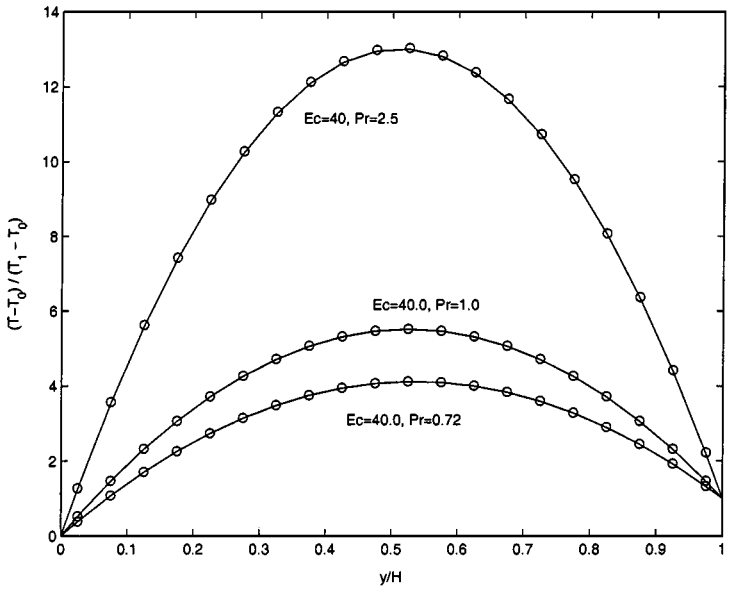

FIG. 5. Temperature ratio $(T - T_0)/(T_1 - T_0)$ in the Couette flow in the low Mach number case $M = 0.1$. The solid line is the analytic solution given by Eq. (31), and the circles are the numerical results from the BGK scheme. While the Eckert number is fixed to 40, the Prandtl number takes the values 2.5, 1.0, and 0.72. The collision time τ used in this scheme is about $0.1\Delta t$.

analytic solution in the compressible case [23],

$$\frac{\tau_w y}{\mu_\infty U} = \frac{u}{U} + Pr\frac{\gamma - 1}{2}M_\infty^2\left[\frac{u}{U} - \frac{1}{3}\left(\frac{u}{U}\right)^3\right],$$

where U is the horizontal velocity of the upper wall and M_∞ is the corresponding Mach

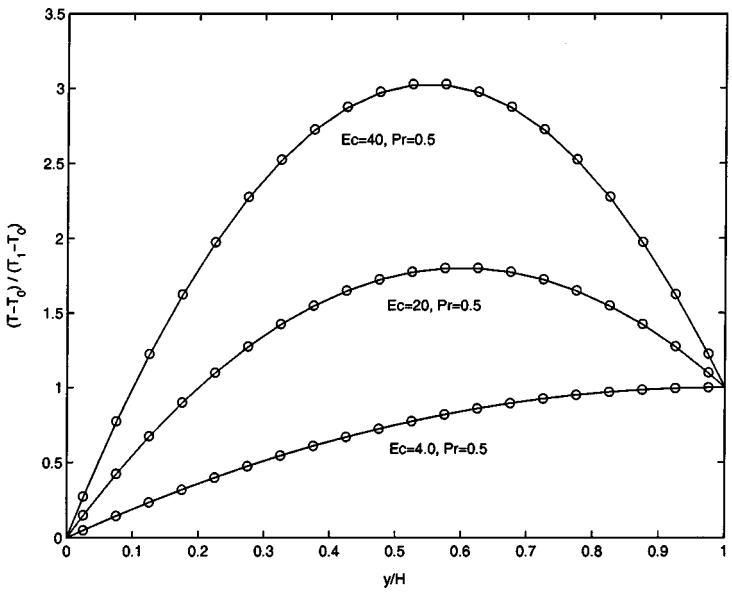

FIG. 6. Continuation of Fig. 5. While the Prandtl number is fixed to 0.5, the Eckert number takes the values 40.0, 20.0, and 4.0.

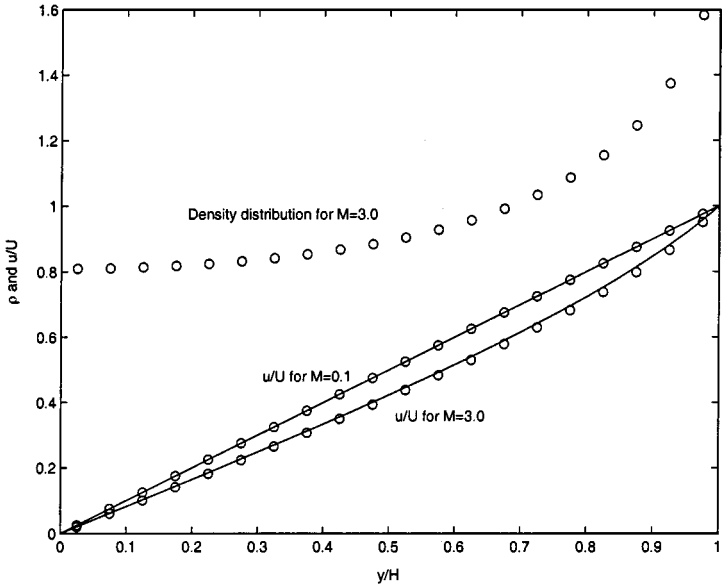

FIG. 7. Velocity u/U and density ρ distributions in high speed Couette flow case for a gas with $Pr = 2/3$ and $\mu \sim T$, where the up-plate is moving with a speed of $M = 3.0$ and the lower boundary has $q_w = 0$. The solid line is the analytic solution given in [23]. As a reference, the solution for $M = 0.1$ is also included.

number. In order to further test the BGK scheme, we have set up the upper and lower boundary conditions with $M_\infty = 3.0$, $q_w = 0$, and Prandtl number $Pr = 2/3$. The viscosity coefficient is set to be $\mu \sim T$. The same number of 20 mesh points is used. The simulation result for the velocity distribution in the channel is shown in Fig. 7, where the solids line is the exact solution from the above formula. In order to see clearly the compressibility, the density distribution in the channel is also included in Fig. 7, from which we can observe the large density variation close to the upper boundary. Also, as a reference, the velocity distribution at a low Mach number case $M_\infty = 0.1$ is included, which reduces to a nearly linear profile.

Case 2. *Navier–Stokes Shock Structure*

This is also a 1D case, which is mainly to test the performance of the BGK scheme from the shock capturing to shock structure calculation. The initial condition is that a stationary shock with Mach number $M = 1.5$ is located at $x = 0$. The kinematic viscosity coefficient for the Navier–Stokes equations takes a value $\nu = 0.00025$, which corresponds approximately to a shock thickness, $l_s \sim 1/300$. We have tested six cases with different cell size, which range from the under-resolved case with $\Delta x = 1/100$ to the well-resolved case with $\Delta x = 1/3200$. The density distributions are shown in Fig. 8, where the solid line is the exact NS solution with $Pr = 1.0$ and $\gamma = 1.4$. From the coarse mesh to fine mesh cases, the shock structure gradually appears and it does converge to the exact Navier–Stokes solution. In the coarse mesh case, the BGK scheme could capture the shock jump crisply without any oscillation. Since the physical collision time τ is determined by Eq. (22), with the change of the cell size, the maximum ratio of $\tau/\Delta t$ ranges approximately from 0.3 to 10 through these cases. We have also tested the schemes based on Eqs. (23) and (24) in the

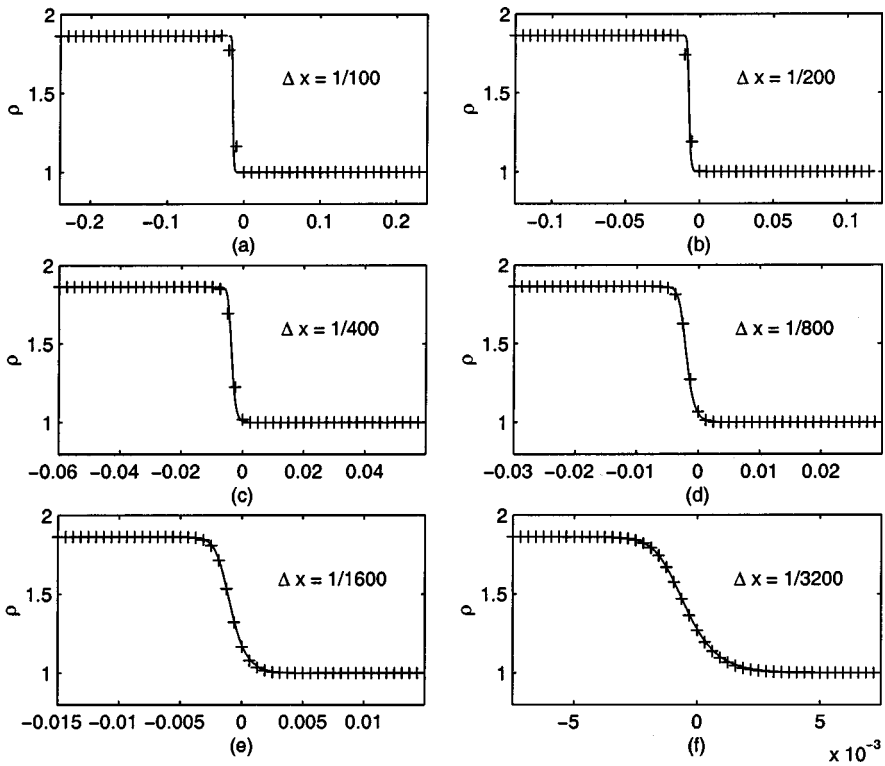

FIG. 8. Density distributions of a stationary shock wave with $M = 1.5$. The kinetic viscosity coefficient of the flow is $\nu = 0.00025$, which corresponds to a shock thickness $l_s \sim 1/300$. The numerical solution (+ sign) is obtained from the BGK scheme with different cell sizes. The solid lines are the exact Navier–Stokes solution. The cell sizes used are (a) 1/100, (b) 1/200, (c) 1/400, (d) 1/800, (e) 1/1600, and (f) 1/3200.

above shock structure calculation. Both methods give almost identical NS solutions in this case, which is consistent with the observation in [8].

In order to further test the BGK scheme for the Navier–Stokes solutions, in the following we are going to calculate the shock structure for a monatomic gas with $\gamma = 5/3$ and a viscosity coefficient $\mu \sim T^{0.8}$. These cases with Mach numbers $M = 1.5$ and 10.0, and Prandtl number $Pr = 1.0$ and $Pr = 2/3$ are tested. The reference "exact solution" of the shock structure is obtained by solving the NS equations using the Matlab programs included in Appendix C. In all cases, the dynamic viscosity coefficient at the upstream keeps a constant $\mu_{-\infty} = 0.0005$. Because the normal stress and the heat flux seem to show the greatest numerical sensitivity, these are selected also to display. Figures 9–16 show the temperature T and the fluid velocity u profiles across the shock layer, as well as the normal stress and the heat flux defined by

$$\tau_{nn} = \frac{4}{3}\mu u_x/2p, \quad q_x = -\frac{5}{4}\frac{\mu}{Pr}T_x/pc,$$

versus fluid velocity $u/U_{-\infty}$. In the calculations, the mesh size is $\Delta x = 1/1600$ for the $M = 1.5$ case and $\Delta x = 1/800$ for the $M = 10.0$ case. The solid lines are the exact solutions. Even with a high degree of nonequilibrium, the Navier–Stokes shock structure is basically captured by the BGK scheme. Notice that there is a great sensitivity of τ_{nn} and q_x in the

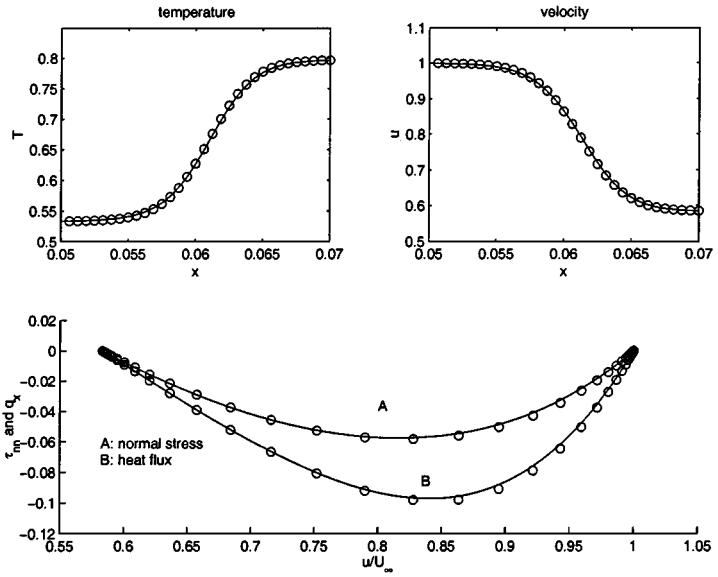

FIG. 9. Shock structure calculations for a monatomic gas with $\gamma = 5/3$, $M = 1.5$, $Pr = 1.0$, and $\mu \sim T^{0.8}$. The plots include temperature T and velocity u distributions inside the shock layer, as well as the normal stress τ_{nn} and the heat flux q_x. The solid lines are the "exact" solutions obtained in Appendix C. The van Leer limiter is used in the initial data reconstruction.

Mach number 10 case when using the van Leer limiter. Even though the temperature and velocity distributions are very close to the Navier–Stokes solutions, the normal stress and heat flux have certain deviations in the location with the highest velocity and temperature gradients. If the nonlinear limiter is not implemented in this well-resolved case, such as using Eq. (1) for the flow interpolation at a cell interface, the shock structures obtained

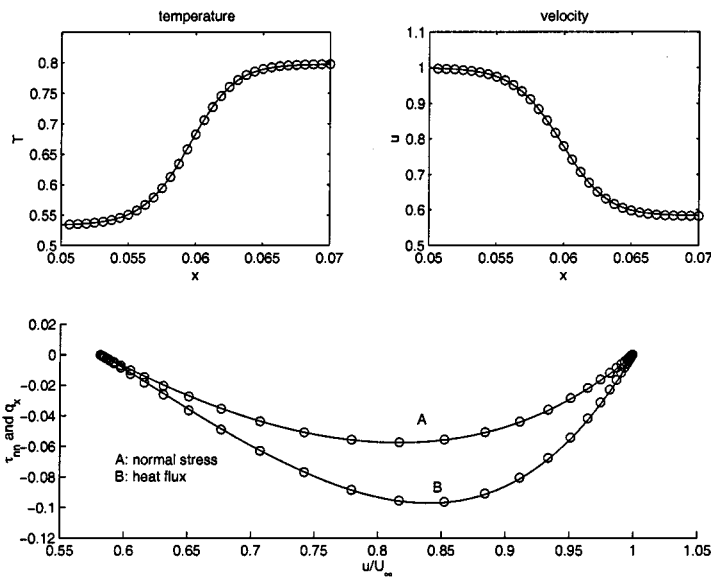

FIG. 10. Same as Fig. 9 except the absence of no-limiter in the initial data reconstruction (1).

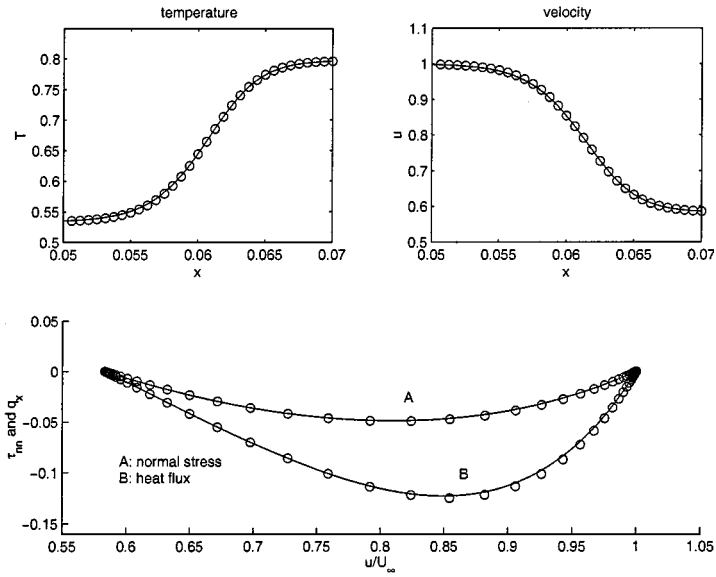

FIG. 11. Continuation of Fig. 9 for a gas with $\gamma = 5/3$, $M = 1.5$, $Pr = 2/3$, and $\mu \sim T^{0.8}$. The van Leer limiter is used in the initial data reconstruction.

from the BGK scheme match with the exact solutions excellently, such as those shown in Figs. 10, 12, 14, and 16.

From these test cases, we can see that the BGK scheme basically gives a good NS solution from the near equilibrium to highly nonequilibrium flows. The Prandtl number fix introduces correct dynamical effect on the thermal flow motion.

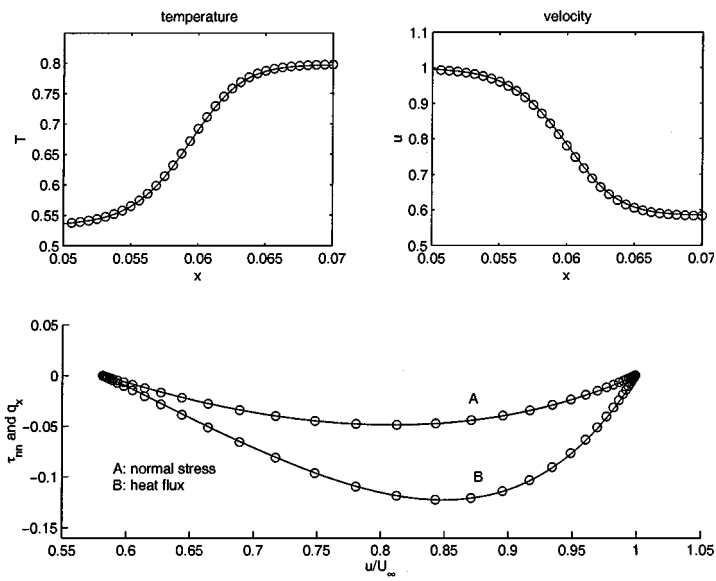

FIG. 12. Same as Fig. 11 except the absence of no-limiter in the initial data reconstruction (1).

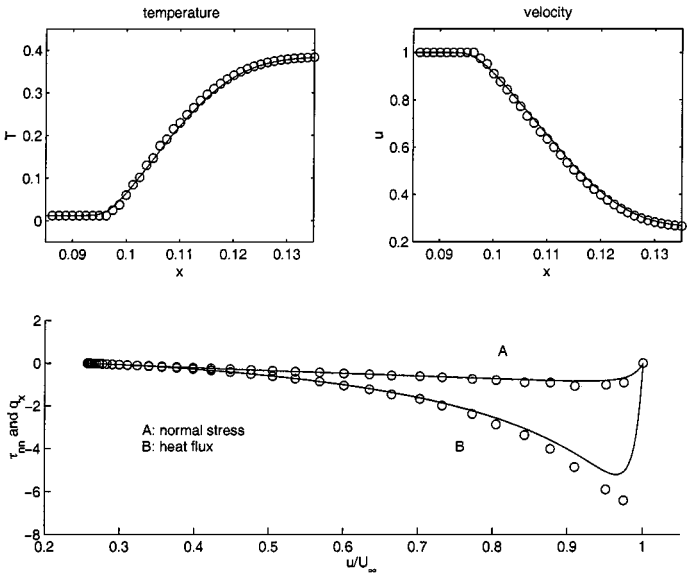

FIG. 13. Highly nonequilibrium shock structure calculation for a gas with $\gamma = 5/3$, $M = 10.0$, $Pr = 1.0$, and $\mu \sim T^{0.8}$. The van Leer limiter is used in the data reconstruction.

Case 3. *Mach* 3 *Step Problem*

The 2D Mach 3 step problem was first proposed by Woodward and Colella [45]. The computation is carried out on a uniform mesh with 120×40 cells, and the cell size used is $\Delta x = \Delta y = 1/40$. In order to test the viscous effect on the flow structure, we have used a different Reynolds number $\mathrm{Re} = UL/\nu = 10^5, 10^3, 50$, where the length scale is $L = 1.0$ and the upstream velocity is $U = 3.0$. The adiabatic slip Euler boundary condition is

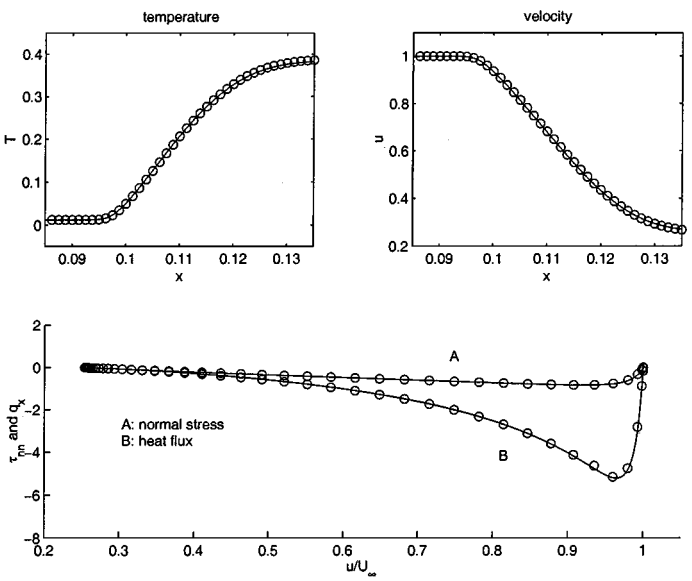

FIG. 14. Same as Fig. 13 except the absence of no-limiter in the initial data reconstruction (1).

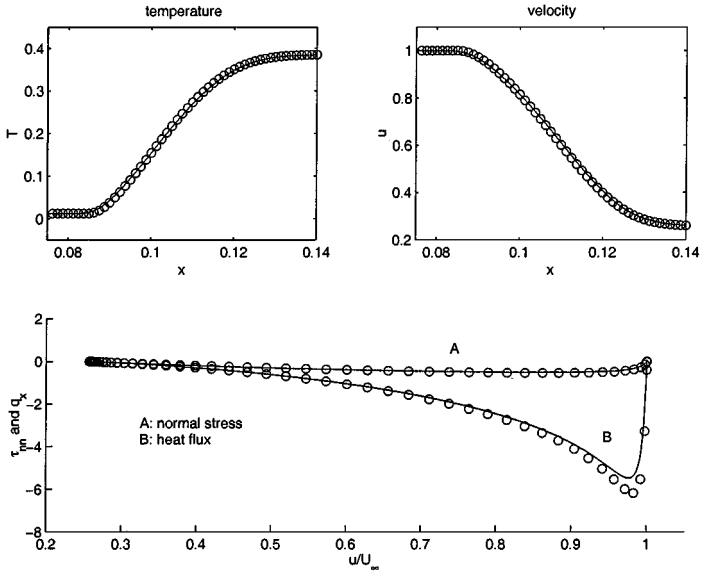

FIG. 15. Continuation of Fig. 13 for a gas with $\gamma = 5/3$, $M = 10.0$, $Pr = 2/3$, and $\mu \sim T^{0.8}$. The van Leer limiter is used in the initial data reconstruction.

imposed at the boundaries in order to avoid the formation of viscous boundary layer. The density and pressure distributions at a different Reynolds number are presented in Figs. 17–19. From these figures, we can clearly observe the effect of viscosity coefficient on the flow structure, such as the shear layer and the shock wave structure. Especially, in the case with $\mathrm{Re} = 50$, the shock structure is well resolved. At the low Re, the molecular transport processes influence essentially the whole of the perturbed flow field, which deviates from

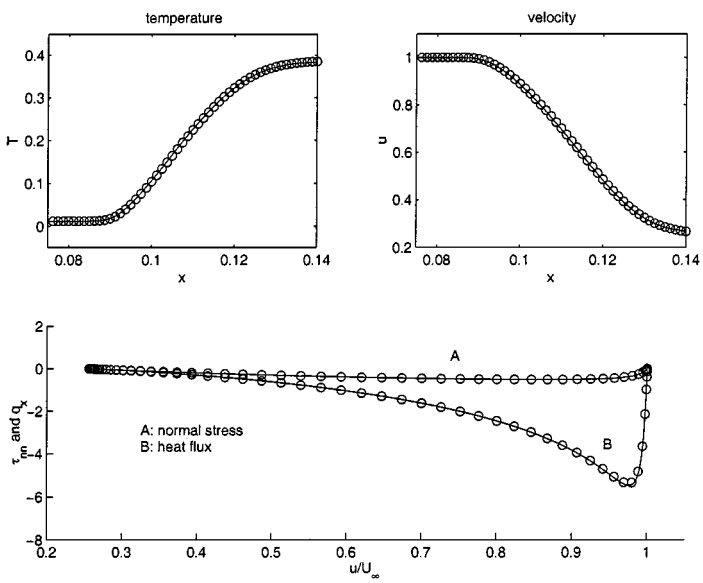

FIG. 16. Same as Fig. 15 except the absence of no-limiter in the initial data reconstruction (1).

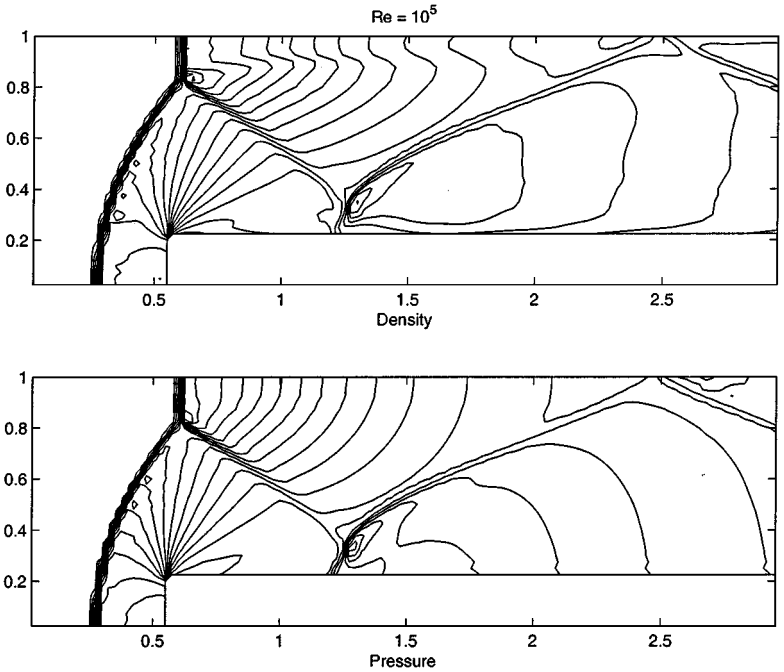

FIG. 17. Density and pressure contours of Mach 3 step problem on a mesh with 120×40 grid points. The Reynolds number used in this case is $\mathrm{Re} = 10^5$ w.r.t. the upstream velocity $U = 3.0$ and the channel height $L = 1.0$. The solution is very close to the solution from the Euler solvers. No special treatment is applied around the step corner.

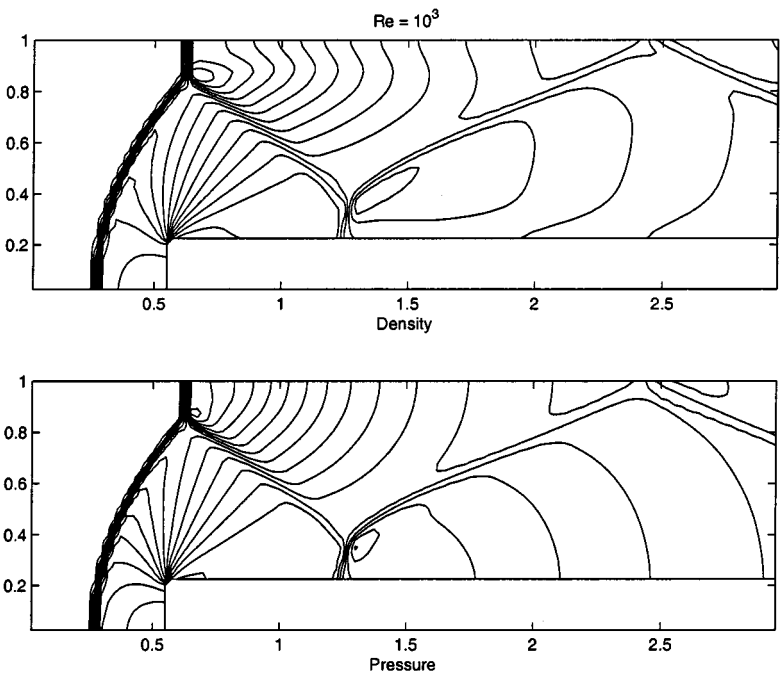

FIG. 18. Density and pressure contours of the step problem with $\mathrm{Re} = 10^3$. Because of the larger viscosity, the shear layer is smeared.

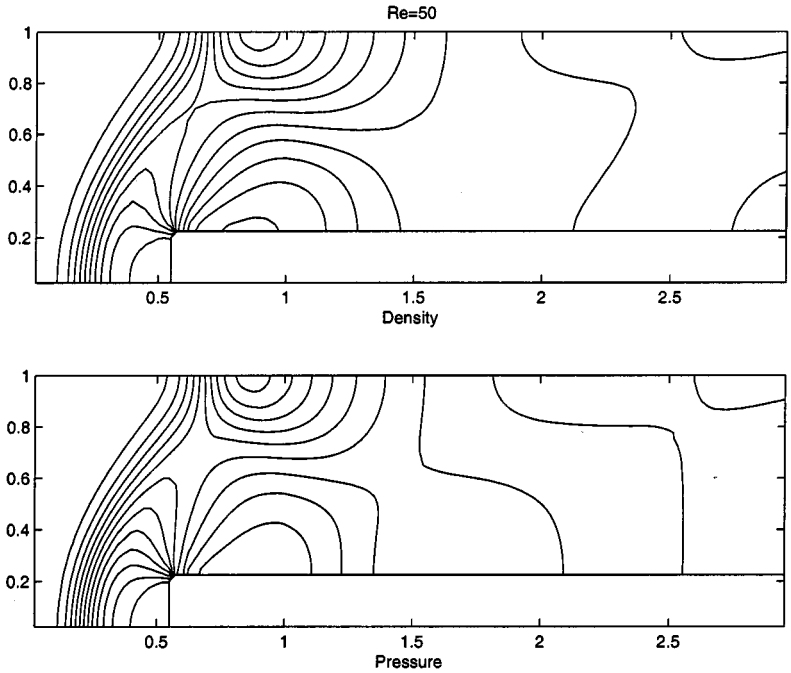

FIG. 19. Density and pressure contours in the case with $Re = 50$. The flow pattern becomes different from the Euler solutions. The shock structure in front of the step is well resolved.

the continuous flow model. It is interesting to compare the BGK solution and the DSMC simulations in small Knudsen number regime, such as the case of Fig. 14.29 in [2]. Because of the inclusion of the nonequilibrium state and the easy implementation of kinetic slip boundary condition, the BGK scheme does provide a potential method to connect the Euler solution with the rarefied solution through the Navier–Stokes at near continuum regime.

Case 4. *Laminar Boundary Layer Case*

A laminar boundary layer with Mach number $M = 0.15$ and $Re = 10^5$ is tested over a flat plate. A rectangular mesh with 120×30 grid points is used and the mesh distribution in shown in Fig. 20. The U velocity contours at the steady state are shown in Fig. 20. The U and V velocity distributions at the locations $x = 6.438$ and $x = 34.469$ are plotted in Fig. 21, where the solid lines are the exact Blasius solutions in the x- and y-directions. Because of the rectangular mesh, the number of grid points in the boundary layer at different locations are different. In both locations, the numerical solutions fit the exact solution very well. Because of the high Reynolds number in this case, the physical collision time τ determined by the viscosity coefficient is much smaller than the time step Δt, i.e., $\tau \ll \Delta t$. For this case, the previous BGK schemes could also capture the boundary solution correctly [46]. The results presented in Fig. 12 of [5] about the BGK scheme are due to the misuse of the viscous term in the Chapman–Enskog expansion as stated earlier.

When Eqs. (23) and (24) are used for the flux calculation in the above boundary layer case, the simulation results are shown in Fig. 22. For the time accurate collisionless Boltzmann solution (23), the effective viscous coefficient is approximately proportional to $(\mu_{phys} + \Delta tp/2)$, where μ_{phys} is the physical viscosity coefficient and $\Delta t/2$ is coming from the free transport mechanism. For the first-order time accurate and second-order

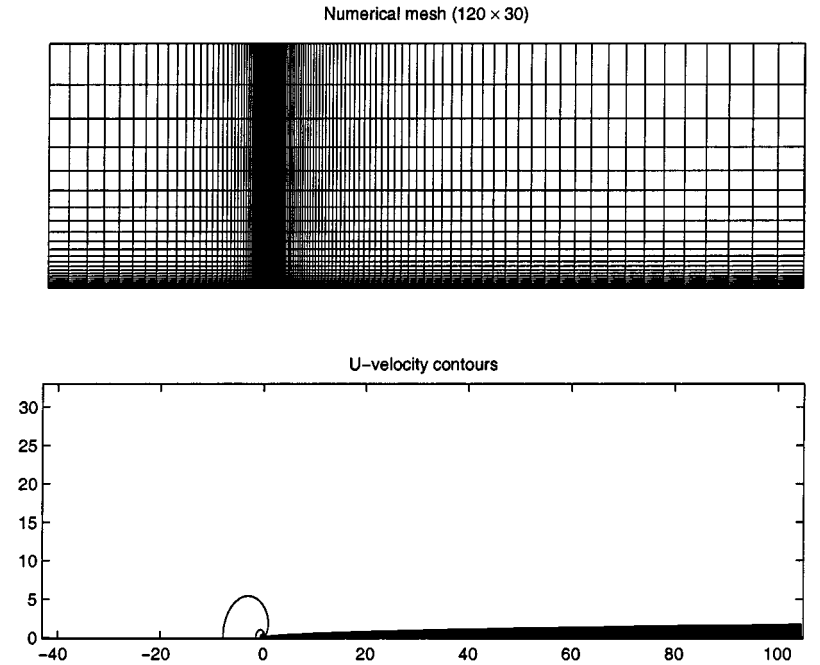

FIG. 20. Upper: Numerical mesh with 120 × 30 grid points for the boundary layer calculation. Lower: U velocity contours at $\mathrm{Re} = 10^5$.

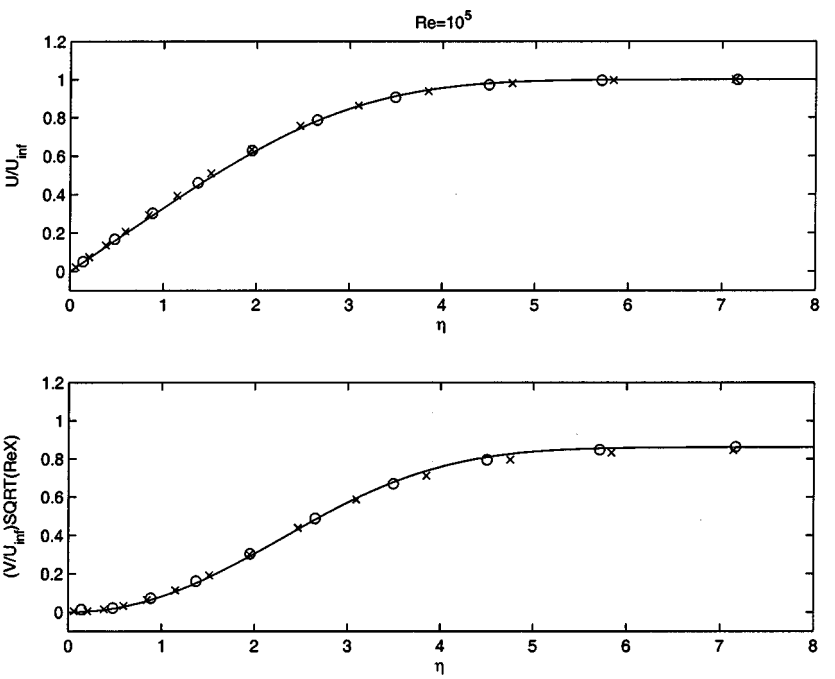

FIG. 21. Continuation of Fig. 20. U (upper) and V (lower) velocity distributions along the vertical lines at $x = 6.438$ (circle sign) and $x = 34.469$ (cross sign) in the case with $\mathrm{Re} = 10^5$. The solid lines are the exact Blasius solutions of U and V velocities.

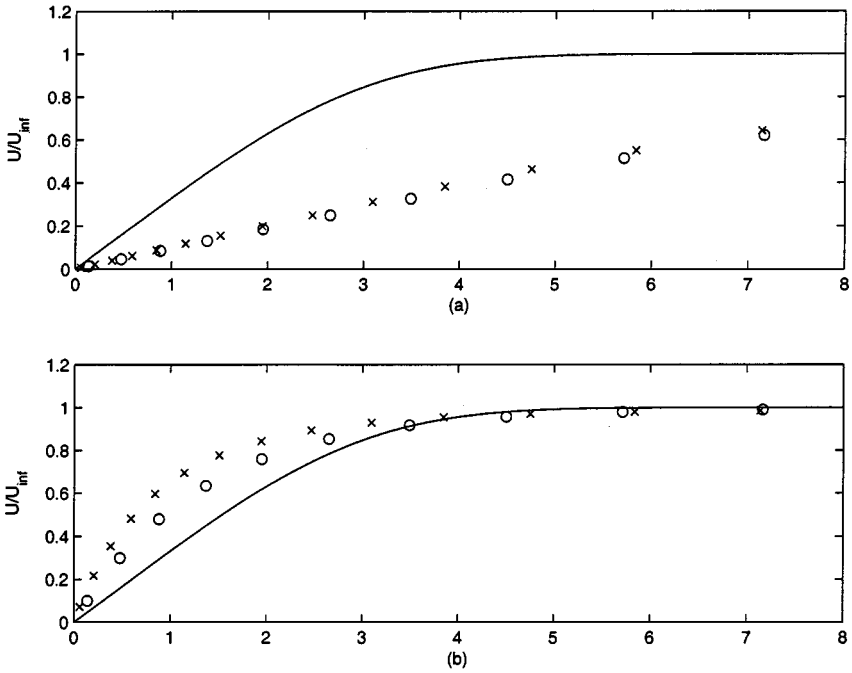

FIG. 22. U velocity distributions from the KFVS NS schemes: (a) Eq. (23) and (b) Eq. (24).

space accurate scheme (24), the viscosity coefficient of the scheme is roughly proportional to $(\mu_{phys} - \Delta t p/2)$, where the forward Euler time steping introduces an antidiffusive term $(\sim -\Delta t p)$. Therefore, the solution in Fig. 22a is more diffusive, and the solution in Fig. 22b is less diffusive than the physical solution determined by μ_{phys}. Because of the stretched mesh, initial data reconstruction, and directional splitting, Eqs. (23) and (24) have complicated dissipative nature. The above effective viscosity estimates are only from the physical intuition. As we can see from Fig. 22, the similarity solution is even lost. This means that the effective dissipative coefficient depends on local mesh size.

Case 5. *Shock Boundary Layer Interaction*

This test is about the interaction of an oblique shock at an angle 32.6° with a boundary layer. The Mach number of the shock wave is $M = 2.0$ and the Reynolds number for the upstream flow is $\mathrm{Re} = 2.96 \times 10^5$. The dynamical viscosity μ used here is the Sutherland's law, and the Prandtl number is equal to 0.72. A mesh similar to Fig. 20 with 110×60 grid points is constructed. The skin friction and pressure distributions at the surface of the plate is shown in Fig. 23, where the data $*$ is the experimental data from [13]. The pressure contours in the whole computational domain are shown in Fig. 24. Because of the high Reynolds number, the shock structure is not well resolved in this case. So, in terms of the shock, it is only a shock capturing scheme. But, in terms of the boundary layer, it is a Navier–Stokes solver because the boundary layer is well resolved. In this test, the condition $\tau < \Delta t$ is satisfied. The previous BGK scheme works also. The numerical solution from the previous BGK scheme is shown in [47]. However, for the KFVS and FVS schemes, the numerical dissipation could easily poison the boundary layer solution, since their validity condition is $\mu/p \gg \Delta t$.

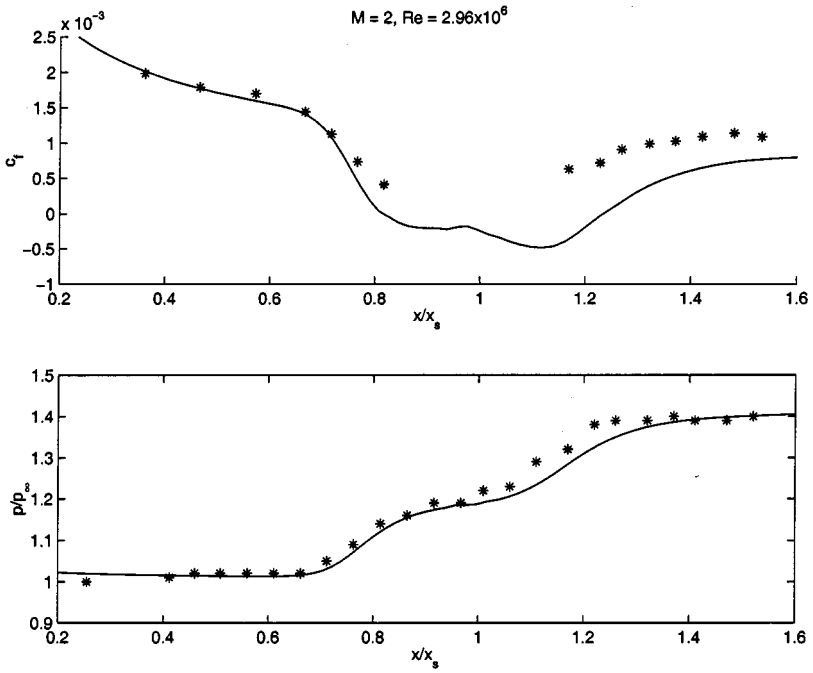

FIG. 23. Shock-boundary interaction case. (upper) skin friction; (lower): pressure distribution, along the flat plate. The $*$ is the experimental data [13]. Solid line: numerical solution on a mesh of 110×60 grid points.

4. ARTIFICIAL DISSIPATION—GODUNOV—BGK METHOD

4.1. *Dynamical and Kinematical Dissipation*

In order to represent a physical solution in a discretized space, the numerical representation depends closely on the relative scales of the mesh size and the physical flow structure. For a physical solution determined by μ_{phys} (Fig. 25), the discretized flow representation

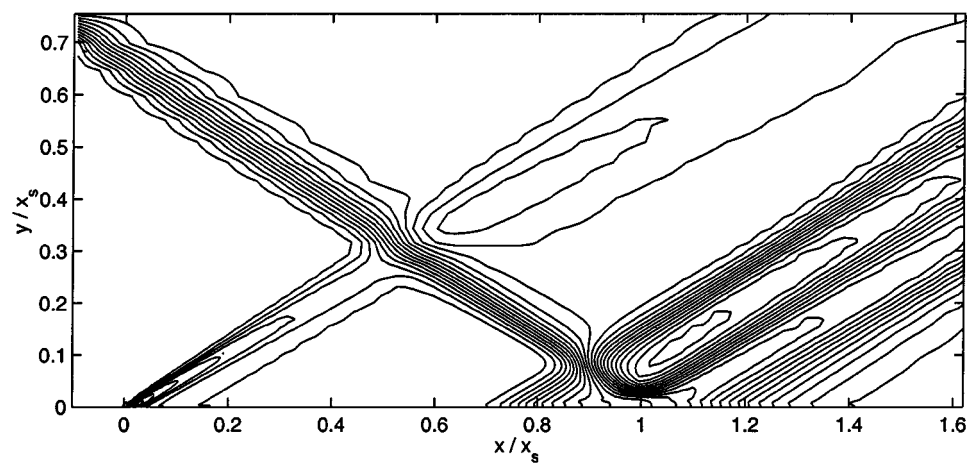

FIG. 24. Pressure contours in the shock-boundary layer interaction case.

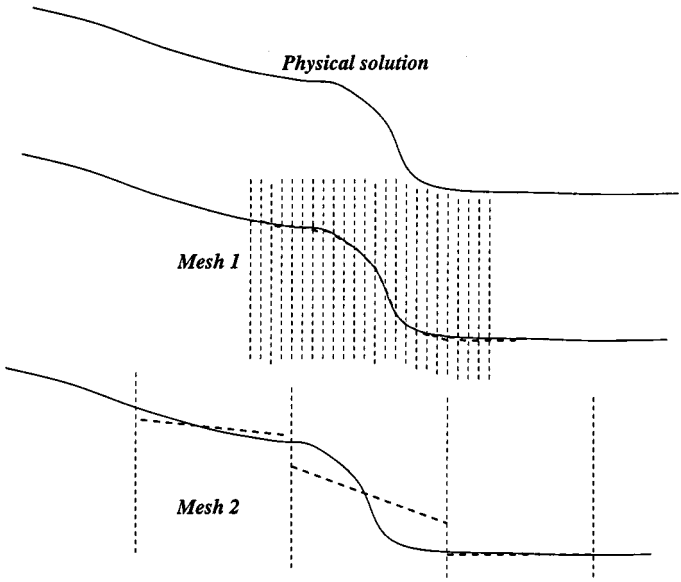

FIG. 25. Numerical representation of the same physical solution in two mesh with different cell sizes.

depends on the mesh size used. In mesh 1, where the mesh size is much smaller than the thickness of the physical structure, any consistent scheme should present an accurate solution. However, with the use of a coarse mesh, such as mesh 2 in Fig. 25, phenomena which are not included in the original physical solution appear. Two considerations have to be taken into account correctly to represent the numerical fluid in mesh 2. Firstly, the physical structure is replaced by a numerical one with the thickness of the cell size. Secondly, discontinuities appear at the cell interface.

In the CFD algorithm development, the above two factors have been considered separately. Two classical pioneering papers for the shock capturing schemes are by von Neumann and Richtmyer [44] and by Godunov [12]. von Neumann and Richtmyer realized the first factor and compensated for it by requiring additional numerical dissipation in the governing equations, which would enlarge the shock thickness to the scale of the cell size. As a result, the governing equation for the numerical fluid should be a viscous governing equation and the total dissipative coefficient has two parts, $\mu = \mu_{phys} + \mu_{num}$. This amount of numerical dissipation μ_{num}, which is included in the governing equations, is called the *dynamical* dissipation. After the original idea of von Neumann and Richtmyer, a number of different artificial dissipative terms have been tried by various authors. It is still an active research area to design a general dependence of μ_{num} on the flow distribution.

The success of the Godunov method is that it realizes the factor 2, which introduces a discontinuity at the cell interface in the flow representation. The realization and implementation of a discontinuity become paramountly important, and the dissipation introduced through the averaging in the initial data can be hardly recovered dynamically through a modification of the governing equation [48]. Since the Godunov dissipation is coming purely from the initial data, we will call it as the *kinematic* dissipation.

The introduction of the discontinuities also leads naturally to the incorporation of wave propagation into the numerical scheme, the so-called Riemann solution. When an exact Riemann solution is used in the flux evaluation, it totally ignores the factor 1. In other words,

even though the Godunov method captures the shock properly, but the shock thickness is obtained from the kinematic dissipation, which depends closely on the mesh construction in 2D case [49]. The post-shock oscillations and the shock instabilities can be generated if the shock thickness is obtained from the kinematic dissipation only. For many approximate Riemann solvers, such as those included in [39], resulting from the different wave modeling in the gas evolution stage, the real governing equation underlying the flux construction can be different from the inviscid Euler equations. For example, the KFVS and FVS schemes have a dynamical dissipation $\mu_{num} \sim \Delta t$ in the gas evolution stage. Therefore, the factor 1 is implicitly included in the FVS methods, and the robustness of these schemes is well established. But, on the other hand, this kind of dissipation is implicit and therefore uncontrollable. It may become a hidden harmful factor for the viscous flow simulation. In order to reduce the dynamical dissipation in the flux splitting formulation $F = F^+(U_l) + F^-(U_r)$, many schemes require a high-order interpolation to make the discontinuity between U_l and U_r as small as possible. Some approximate Riemann solvers are even based on irrational approximation, which lacks a rigorous physical model to subsequently improve the schemes. In summary, the development of a robust and accurate scheme depends on the consideration of both dynamical and kinematical dissipation.

4.2. *Reconsideration of Generalized Riemann Solver and TVD Concept*

From the above analysis, we may understand the following consideration. For a second-order scheme with high-order initial interpolation, even with a discontinuity at a cell interface the kinematic dissipation introduced in the initial data could be on the order of $\mu_{num} \sim \Delta x^2$, which is theoretically not enough to construct a numerical shock thickness requiring $\mu \sim \Delta x$. Therefore, *if a generalized Riemann problem (GRP) is precisely solved for the inviscid Euler in the gas evolution stage from the linearly distributed flow variables, where the wave structure may not keep the same structure as the Riemann problem from two constant states, a high-order accurate scheme could not properly capture the numerical shock waves.* Even with a discontinuity at a cell interface, additional dynamical dissipation is needed.

The current successful CFD algorithm design principles for the compressible flow are mainly based on the concepts of Total Variation Diminishing (TVD) [15]. With the definition, $TV(u^n) = \sum_j |u^n_{j+1} - u^n_j|$, the TVD condition says $TV(u^{n+1}) \le TV(u^n)$. It is well known that the TVD method is applicable only to those problems of gas dynamics for which it is known a *priori* that their solutions meet the TVD requirement, such as the linear system or the scalar equation. For such a system, the TVD concept becomes an indispensable tool to justify the shock capturing schemes. For a nonlinear system without TVD properties in its solution, the TVD concept can be applicable truthfully to the initial data reconstruction, such as $TV(\bar{u}^n) \le TV(u^n)$, where u is the cell averaged data and $\bar{u}$ is the reconstructed one. This requirement is similar to the reconstruction technique used in the MUSCL scheme. After the initial reconstruction, the update of flow variables is determined from the governing equation, which is basically fixed once the initial interpolated data is given. So, it seems impossible to design a scheme based on the requirement of its output result in the next time level. Therefore, for the nonlinear system, besides the TVD requirement in the initial data reconstruction, the use of dynamical and kinematical dissipation in the algorithm development becomes necessary. In order to make these concepts clear, let's consider the following example. For the Euler equations, with the initial cell averaged conservative variables w^n_j inside each cell (see Fig. 26), we can reconstruct the initial data simply as the connection

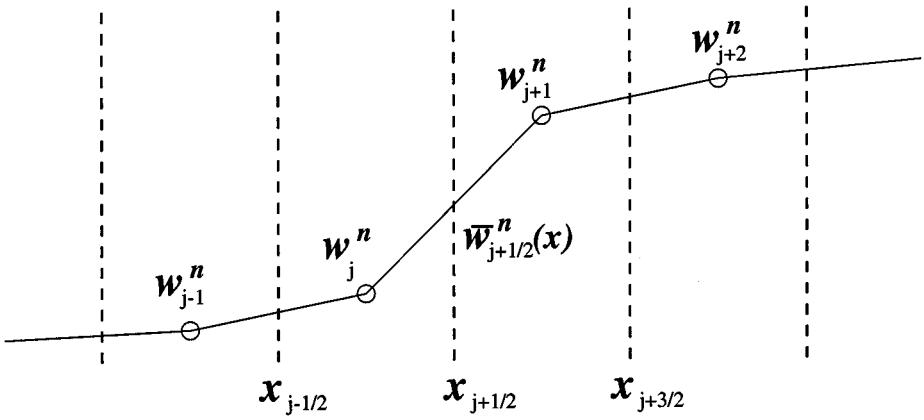

FIG. 26. The reconstructed initial data (solid line) at time step n is simply the connection of the cell averaged values (circles). The fluxes across the cell interface are evaluated based on the initial data $\bar{W}^n_{j+1/2}(x)$, which is linearly distributed for all conservative variables around a cell interface. The Lax–Wendroff-type scheme (32) based on this initial condition is actually an accurate second-order Generalized Riemann Solver for a short time step with CFL number less than 0.5. The simply connected initial data has the same total variation $TV(\bar{W}^n) = TV(W^n)$. No spurious oscillations created in the initial data reconstruction.

of the cell averaged data w^n_j. The reconstructed continuous data satisfy the TVD property, such as

$$TV(\bar{w}^n) = TV(w^n),$$

where $TV(\bar{w}^n) = \int |\bar{w}'|dx$ and $TV(w^n) = \sum |w^n_{j+1} - w^n_j|$, and there is no local extreme created. Note that w represents the mass, momentum, and energy, respectively. After the above initial reconstruction, a conservative scheme in 1D case can be constructed as,

$$w^{n+1}_j = w^n_j + \frac{1}{\Delta x}\int_{t^n}^{t^{n+1}} \left(F_{j-1/2}(t) - F_{j+1/2}(t)\right) dt,$$

where the numerical flux $F_{j+1/2}$ is obtained based on the reconstructed initial data $\bar{w}^n$ and the gas evolution model. Since the flow variables are continuous across each cell interface initially, within a short time step with CFL number less than 0.5, before the waves generated from the corners at the cell center propagate to the cell interface, the Lax–Wendroff gas evolution model is actually an accurate second-order Generalized Riemann Solver. The time-dependent flow variable $\bar{w}_{j+1/2}(t)$ at the cell interface can be obtained as

$$\bar{w}_{j+1/2}(t) = \bar{w}_{j+1/2}(0) + t\frac{\partial \bar{w}}{\partial t}|_{t=0}, \tag{32}$$

where the time derivative of the conservative variables can be evaluated using the reconstructed spatial derivatives. Then, the numerical flux $F_{j+1/2}(t)$ can be obtained from $\bar{w}_{j+1/2}(t)$. Since the initial data satisfy the TVD property for all cosnervative variables and the gas evolution stage is based on an almost exact Generalized Riemann Solver to the second-order accuracy for the Euler Equations, the numerical results are supposed to be reasonable. But, numerically with two CFL numbers 0.25 and 0.85, the solutions

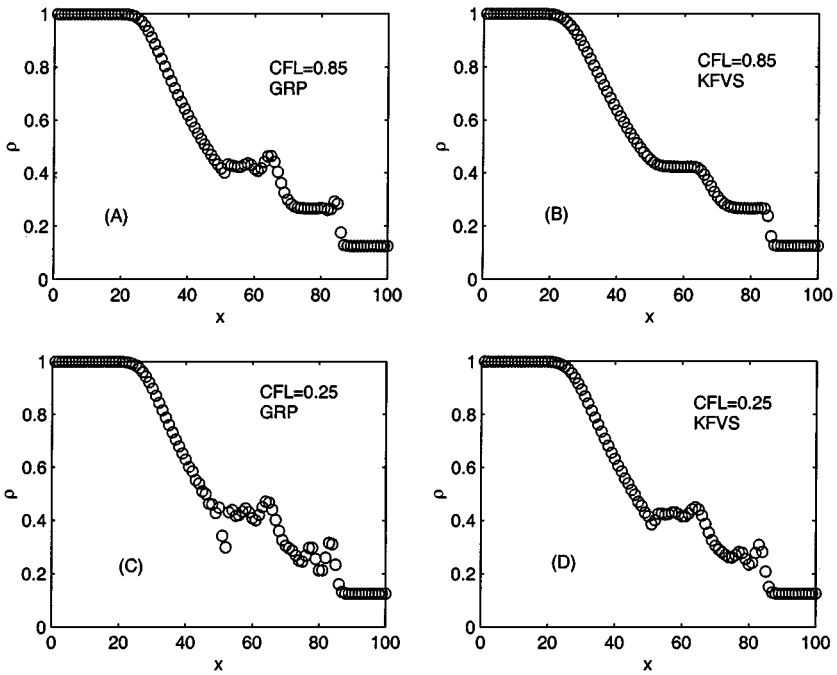

FIG. 27. Generalized Riemann Solutions (GRS) and the KFVS solutions for the Sod test case based on the initial data $\bar{W}$ on Fig. 26. (A) and (C): obtained from Eq. (32) with CFL number 0.85 and 0.25. (B) and (D): from Eq. (33) with CFL number 0.85 and 0.25.

for the Sod test case are shown in Fig. 27A and 27C. Both cases present oscillatory results. This observation can be hardly explained from the TVD concept alone. Based on the dynamical and kinematical dissipation, we can explain the observation in the following: (i) even with the TVD property in the initial data reconstruction, the kinematic dissipation becomes $\mu_{num} \sim (\Delta x)^2$; (ii) in the gas evolution stage, the Euler equations are almost precisely solved without introducing any dynamical dissipation. As a result, the total artificial dissipation is not enough to construct a smooth shock transition, which requires $\mu \sim \Delta x$ in the shock region. Under the same reconstructed initial data in Fig. 26, we also test the time accurate second-order KFVS scheme as an approximate Generalized Riemann Solver. With the initial linear slopes for $\bar{w}$ at a cell interface, the gas distribution function in the KFVS scheme for the Euler equations becomes

$$f_{j+1/2}(t) = f_0(x - ut) = g_{j+1/2}(1 - aut), \tag{33}$$

where $g_{j+1/2}$ is determined from $\bar{w}^n_{j+1/2}(0)$ and $a = a_1 + a_2u + a_3(u^2 + \xi^2)/2$ comes from $\partial\bar{w}/\partial x$. The simulation results based on the KFVS scheme are shown in Fig. 27B and 27D, where the solution is smooth in the large CFL time step and oscillatory for small CFL number one. This observation can be explained from the dynamical and kinematic dissipation concept also: (i) the kinematic dissipation in the initial data is still $\mu_{num} \sim (\Delta x)^2$; (ii) in the gas evolution stage, the KFVS is solving a viscous governing equation with $\mu_{num} \sim \Delta t$. For the large CFL number case, the artificial dynamical dissipation is enough for the smooth shock construction. But, in the small CFL number case, the dissipation

which is proportional to the time step is not adequate. From this example, we can see that for the nonlinear system, a TVD concept alone is not enough to explain the numerical observation. A physically reasonable scheme cannot be developed without including both the kinematic and dynamical dissipation. Also, it can be realized that even with a high-order initial nonoscillatory reconstruction, it may not be a good thing that an exact solution of the inviscid equations is used for the flux calculation. Fortunately, many high-resolution schemes always use the first-order dynamical model, such as the fluxes from two constant states. The interpolated slopes do not anticipate the time-dependent gas evolution explicity. For example, for the second-order Hancock method for the Euler equations [39], the time accuracy is obtained by evaluating the cell interface values at half time step. But, in this time evolution process, inside each cell the whole interpolated curve is shifted upward or downward, and there is not any slope steepening mechanism used, even through the steepening mechanism is intrinsic for the nonlinear system. So, the Hancock time accuracy method and many Runge–Kutta methods are dynamically different from the gas evolution model in the Generalized Riemann Solution. Many schemes, such as the central schemes [28, 6], have mixed kinematic and dynamical dissipation in its continuous averaging process because of the mesh shifting (staggered mesh). The analysis of these schemes becomes difficult.

4.3. *Methodology of the BGK Scheme*

In order to develop a rational and robust numerical scheme, both dynamical and kinematical dissipation have to be accounted for, and both factors are actually coupled in certain sense. In other words, the flow discontinuities at the cell interface means under-resolveness of the physical structure and then additional dynamical dissipation in the governing equations becomes necessary. The methodology of the BGK scheme is somehow to combine these two important issues:

(i) a viscous governing equation with an enhanced viscosity coefficient (22), which is proportional to the discontinuity jump, is solved.

(ii) the initial condition includes the possible discontinuity and nonequilibrium state.

In the smooth flow region, the additional numerical viscosity and the discontinuity at the cell interface disappear simultaneously. The BGK scheme goes back to the traditional central schemes for the NS equations. The BGK scheme has both signatures of the Riemann solver and the central scheme through the KFVS part (Eqs. (8) and (23)) and continuous equilibrium part (Eqs. (10) and (21)). These properties emerge and are nonlinearly coupled naturally in the gas evolution process.

In summary, both the explicit dynamical dissipation suggested by von Neumann and Richtmyer and the kinematic dissipation introduced by Godunov through the cell averaging (or interface discontinuity) are important for the algorithm development. Even for the inviscid Euler equations, the numerical scheme is better to be based on the viscous governing equations. As pointed out by P. Roe [34], it is not correct to think of the Godunov flux as a perfect one to which all other formulas are merely simple approximation. It is inappropriate also to regard the gas-kinetic BGK-type scheme as simply an alternative Riemann solver. Whether one uses a Riemann solver or not should not become a criterion about the quality of a numerical scheme. The principles should be based on the correct representation of a physical fluid in a discretized space and follow its correct time evolution, where both the cell size and flow structure have to be considered.

5. CONCLUSION

This paper extends the gas-kinetic BGK scheme to the viscous flow simulations by including a nonequilibrium state in the initial condition of the gas distribution function. As a result, the BGK scheme approximates the Navier–Stokes equations accurately, which is valid in both $\tau < \Delta t$ and $\tau > \Delta t$ regimes. The new scheme works not only in the viscous shear or boundary layer cases with $\tau < \Delta t$. but also in the construction of a Navier–Stokes shock structure with $\tau \gg \Delta t$. The KFVS NS method and KFVS scheme are the limiting cases of the current BGK scheme with the condition $\mu/p \gg \Delta t$, and both schemes are applicable to the Navier–Stokes solutions only under such a limiting condition. Also, the kinetic boundary condition and Prandtl number fix are presented and tested numerically in this paper. The connection among the artificial dissipation, the Godunov method, and the kinetic BGK scheme is discussed. Two concepts, the dynamical and kinematical dissipation for the compressible flow algorithm development, are introduced.

Following previous papers [31, 51, 52], the present paper shows a progressive development of the BGK-type schemes. The comprehensive numerical results presented in this paper and the physical and numerical analysis about the schemes indicate the level of maturity achieved by the gas-kinetic BGK method for the Euler and Navier–Stokes solutions.

APPENDIX A: MOMENTS OF THE MAXWELLIAN DISTRIBUTION FUNCTION

In the gas-kinetic scheme, we need to evaluate moments of a Maxwellian distribution function with bounded and unbounded integration limits. Here, we list some general formulas.

First, the Maxwellian distribution for a 2D flow is

$$g = \rho\left(\frac{\lambda}{\pi}\right)^{\frac{K+2}{2}} e^{-\lambda((u-U)^2+(v-V)^2+\xi^2)},$$

where ξ has K degrees of freedom. Then, by introducing the following notation for the moments of g,

$$\rho\langle \ldots \rangle = \int (\ldots) g du dv d\xi,$$

the general moment formula becomes

$$\langle u^n v^m \xi^l \rangle = \langle u^n \rangle \langle v^m \rangle \langle \xi^l \rangle,$$

where n and m are integers, and l is an even integer (owing to the symmetrical property of ξ). The moments of $\langle \xi^l \rangle$ are

$$\langle \xi^2 \rangle = \left(\frac{K}{2\lambda}\right)$$
$$\langle \xi^4 \rangle = \left(\frac{3K}{4\lambda^2} + \frac{K(K-1)}{4\lambda^2}\right).$$

The values of $\langle u^n \rangle$ depend on the integration limits. If the limits are $-\infty$ to $+\infty$, we have

$$\begin{aligned} \langle u^0 \rangle &= 1 \\ \langle u \rangle &= U \\ &\cdots \\ \langle u^{n+2} \rangle &= U \langle u^{n+1} \rangle + \frac{n+1}{2\lambda} \langle u^n \rangle. \end{aligned}$$

When the integral is from 0 to $+\infty$ as $\langle \ldots \rangle_{>0}$ or from $-\infty$ to 0 as $\langle \ldots \rangle_{<0}$, the error function and the complementary error function, appear in the formulation. Thus, the moments for u^n in the half space are

$$\begin{aligned} \langle u^0 \rangle_{>0} &= \frac{1}{2} \mathrm{erfc}(-\sqrt{\lambda} U) \\ \langle u \rangle_{>0} &= U \langle u^0 \rangle_{>0} + \frac{1}{2} \frac{e^{-\lambda U^2}}{\sqrt{\pi \lambda}} \\ &\cdots \\ \langle u^{n+2} \rangle_{>0} &= U \langle u^{n+1} \rangle_{>0} + \frac{n+1}{2\lambda} \langle u^n \rangle_{>0}. \end{aligned}$$

and

$$\begin{aligned} \langle u^0 \rangle_{<0} &= \frac{1}{2} \mathrm{erfc}(\sqrt{\lambda} U) \\ \langle u \rangle_{<0} &= U \langle u^0 \rangle_{<0} - \frac{1}{2} \frac{e^{-\lambda U^2}}{\sqrt{\pi \lambda}} \\ &\cdots \\ \langle u^{n+2} \rangle_{<0} &= U \langle u^{n+1} \rangle_{<0} + \frac{n+1}{2\lambda} \langle u^n \rangle_{<0}. \end{aligned}$$

The same formulation can be obtained for $\langle v^m \rangle$ by changing U to V in the above moments of $\langle u^n \rangle$.

APPENDIX B: SOLUTION OF MATRIX EQUATION $\mathbf{b} = \boldsymbol{M}\mathbf{a}$

In the gas-kinetic scheme, the solution of the following equations is used many times,

$$\begin{pmatrix} b_1 \\ b_2 \\ b_3 \\ b_4 \end{pmatrix} = \boldsymbol{M} \begin{pmatrix} a_1 \\ a_2 \\ a_3 \\ a_4 \end{pmatrix}, \tag{34}$$

where $\mathbf{b}$ and $\boldsymbol{M}$ are known. The matrix $\boldsymbol{M}$ is from the integration of a Maxwellian, i.e., $M_{\alpha\beta} = \int \psi_\alpha \psi_\beta g d\Xi/\rho$, and has the form

$$\boldsymbol{M} = \begin{pmatrix} 1 & U & V & \mathcal{B}_1 \\ U & U^2 + 1/2\lambda_l & UV & \mathcal{B}_2 \\ V & UV & V^2 + 1/2\lambda_l & \mathcal{B}_3 \\ \mathcal{B}_1 & \mathcal{B}_2 & \mathcal{B}_3 & \mathcal{B}_4 \end{pmatrix},$$

where

$$\mathcal{B}_1 = \frac{1}{2}(U^2 + V^2 + (K+2)/2\lambda),$$
$$\mathcal{B}_2 = \frac{1}{2}(U^3 + V^2 U + (K+4)U/2\lambda),$$
$$\mathcal{B}_3 = \frac{1}{2}(V^3 + U^2 V + (K+4)V/2\lambda)$$

and

$$\mathcal{B}_4 = \frac{1}{4}((U^2+V^2)^2 + (K+4)(U^2+V^2)/\lambda + (K^2+6K+8)/4\lambda^2).$$

Defining

$$R_4 = 2b_4 - \left(U^2 + V^2 + \frac{K+2}{2\lambda}\right)b_1,$$
$$R_3 = b_3 - Vb_1,$$
$$R_2 = b_2 - Ub_1,$$

the solution of Eq. (34) is

$$a_4 = \frac{4\lambda^2}{K+2}(R_4 - 2UR_2 - 2VR_3),$$
$$a_3 = 2\lambda R_3 - VR_4,$$
$$a_2 = 2\lambda R_2 - UR_4,$$

and

$$a_1 = b_1 - Ua_2 - Va_3 - \frac{1}{2}a_4\left(U^2 + V^2 + \frac{K+2}{2\lambda}\right).$$

APPENDIX C: MATLAB PROGRAM FOR THE SHOCK STRUCTURE CALCULATIONS

It is well known that the NS equations do not give a physically realistic profile for the strong shock waves. However, in this paper we are mainly interested in the accuracy of the proposed BGK scheme in the capturing of the NS solutions. In order to get a good

reference shock structure, we have used the method suggested by Gilbarg and Paolucci [11] to solve the following NS equations for a stationary shock,

$$\begin{pmatrix} \rho U \\ \rho U^2 + p \\ (E+p)U \end{pmatrix}_x = \begin{pmatrix} 0 \\ \frac{4}{3}\mu U_x \\ \frac{5}{4}\frac{\mu}{Pr}T_x + \frac{4}{3}\mu U U_x \end{pmatrix}_x,$$

with the parameters $\gamma = 5/3$, $\mu \sim T^{0.8}$, $\mu_{-\infty} = 0.0005$, and Prandtl numbers $Pr = 1.0$ and $Pr = 2/3$. With the mass, momentum, and energy conservation through a shock layer, i.e.,

$$\rho U = A$$
$$\rho U^2 + \frac{\rho}{2}T - \frac{4}{3}\mu U_x = B,$$
$$\frac{1}{2}\rho\left(U^3 + \frac{5}{2}UT\right) - \frac{5}{4}\frac{\mu}{Pr}T_x - \frac{4}{3}\mu U U_x = C,$$

where A, B and C are constants, and the following ODEs for the shock structure can be derived,

$$u_x = -\frac{3}{4\mu}\left[B - Au - \frac{AT}{2u}\right]$$
$$T_x = \frac{4Pr}{5\mu}\left[-\frac{1}{2}Au^2 + \frac{3}{4}AT - C + Bu\right],$$

where $\mu = \mu_{-\infty}(T/T_{-\infty})^{0.8}$. The upstream and downstream Rankine–Hugoniot shock conditions are

$$\begin{pmatrix} \rho \\ U \\ p \end{pmatrix}_{-\infty} = \begin{pmatrix} 1.0 \\ 1.0 \\ \frac{1}{\gamma M^2} \end{pmatrix}, \quad \begin{pmatrix} \rho \\ U \\ p \end{pmatrix}_{\infty} = \begin{pmatrix} \frac{(\gamma+1)M^2}{2+(\gamma-1)M^2} \\ \frac{\gamma-1}{\gamma+1} + \frac{2}{(\gamma+1)M^2} \\ \left(\frac{2\gamma}{\gamma+1}M^2 - \frac{\gamma-1}{\gamma+1}\right)\frac{1}{\gamma M^2} \end{pmatrix}.$$

For an easy reference for the future use about the NS shock structure calculation, in the following the Matlab programs solving the above ODEs are included. The integration path is from downstream ($+\infty$) to upstream ($-\infty$). Since adaptive mesh technique is used in the Matlab ODE solver, the shock structure solution obtained is very accurate. The output data include u, T, u_x, T_x, μ, p, and the normal stress and heat flux defined by

$$\tau_{nn} = \frac{4}{3}\mu u_x/2p, \quad q_x = -\frac{5}{4}\frac{\mu}{Pr}T_x/2pc.$$

Shock.m

```
M=1.5; %mach number
gamma=5/3;
Pr=2/3;

%upstream states:
r1=1.0;
u1=1.0;
```

```
mu1=0.0005;
p1=1/gamma/M^2;
T1=2*p1/r1;

%downstream states:
r2=(gamma+1)*M^2/(2+(gamma-1)*M^2)*r1;
u2=((gamma-1)/(gamma+1)+2/(gamma+1)/M^2)*u1;
p2=(2*gamma/(gamma+1)*M^2-(gamma-1)/(gamma+1))*p1;
T2=2*p2/r2;

%conservations:
A=r1*u1;
B=r1*u1^2+p1;
C=(1/2*r1*u1^2+p1/(gamma-1)+p1)*u1;

%ODE solver:
y0=[T2; -u2*(1+eps)]; %downstream states [T2; -U2]
tspan=[0 0.25]; %x=-tspan, solve from downstream to upstream
options = odeset('RelTol',1e-6,'AbsTol',[1e-9 1e-9]);
[t, y]=ode45('Fb,' tspan, y0, options);

x=-t;
T=y(:,1);
u=-y(:,2);

mu=mu1*(T/T1).^0.8;
ux=-3/4./mu.*(B-A*u-1/2*A*T./u); %U_x
Tx=4/5*Pr./mu.*(-1/2*A*u.^2+3/4*A*T-C+B*u); %T_x
r=A./u; %density
p=r.*T/2; %pressure

%plot T and u:

figure(1)
plot(x,T)
xlabel('x')
ylabel('T')

figure(2)
plot(x,u)
xlabel('x')
ylabel('U')

% output:

out(:,1)=x;
out(:,2)=T;
save t out -ascii %save [x T] in file 't'

out(:,1)=x;
out(:,2)=u;
save u out -ascii %save [x U] in file 'u'
```

```
out(:,1)=x;
out(:,2)=p;
save p out -ascii %save [x p] in file 'p'

out(:,1)=x;
out(:,2)=r;
save r out -ascii %save [x rho] in file 'r'

out(:,1)=x;
out(:,2)=mu;
save mu out -ascii %save [x mu] in file 'mu'

out(:,1)=x;
out(:,2)=ux;
save ux out -ascii %save [x U_x] in file 'ux'

out(:,1)=x;
out(:,2)=Tx;
save tx out -ascii %save [x T_x] in file 'tx'

out(:,1)=x;
out(:,2)=4/3*mu.*ux./(2*p);
save v out -ascii %save in file 'v'

out(:,1)=x;
out(:,2)=5/4/Pr*mu.*Tx./p./sqrt(gamma*T/2);
save h out -ascii %save in file 'h'
```

Fb.m

```
function dy=Fb(t,y)
%y(1): T
%y(2): -U
%t: -x
M=1.5; %mach number
gamma=5/3;
Pr=2/3;
%upstream states:
r1=1.0;
u1=1.0;
mu1=0.0005;
p1=1/gamma/M^2;
T1=2*p1/r1;
A=r1*u1;
B=r1*u1^2+p1;
C=(1/2*r1*u1^2+p1/(gamma-1)+p1)*u1;
mu=mu1*(y(1)/T1)^0.8;
%mu=mu1;
dy=[0;0];
dy(1)=4/5*Pr/mu*(1/2*A*y(2)^2-3/4*A*y(1)+C+B*y(2)); % -T_x
dy(2)=3/4/mu*(-B-A*y(2)-1/2*A*y(1)/y(2)); % U_x
```

ACKNOWLEDGMENTS

The author thanks the reviewers for their critical comments and helpful suggestions, and Prof. W. H. Hui for helpful discussion about the physical understanding of numerical schemes. This research was supported in part by the National Aeronautics and Space Administration under NASA Contract NAS1-97046 while the author was in residence at the Institute for Computer Applications in Science and Engineering (ICASE), NASA Langley Research Center, Hampton, VA 23681-2199. Additional support was provided by Hong Kong Research Grant Council through RGC HKUST6132/00P.

REFERENCES

1. P. L. Bhatnagar, E. P. Gross, and M. Krook, A model for collision processes in gases I: Small amplitude processes in charged and neutral one-component systems, *Phys. Rev.* **94**, 511 (1954).
2. G. A. Bird, *Molecular Gas Dynamics and the Direct Simulation of Gas Flows* (Oxford Univ. Press, Inc., New York, 1994).
3. J. P. Boris and D. L. Book, Flux-corrected transport. I. SHASTA, a fluid transport algorithm that works, *J. Comput. Phys.* **11**, 38 (1973).
4. C. Cercignani, *Rarefied Gas Dynamics* (Cambridge University Press, Cambridge, MA, 2000).
5. D. Chae, C. Kim, and O. Rho, Development of an improved gas-kinetic BGK scheme for inviscid and viscous flows, *J. Comput. Phys.* **158**, 1 (2000).
6. S. C. Chang, The method of space-time conservation element and solution element—A new approach for solving the Navier–Stokes and Euler equations, *J. Comput. Phys.* **119**, 295 (1995).
7. S. Chen and G. Doolen, Lattice Boltzmann method for fluid flows, *Ann. Rev. Fluid Mech.* **30**, 329 (1998).
8. S. Y. Chou and D. Baganoff, Kinetic flux-vector splitting for the Navier–Stokes equations, *J. Comput. Phys.* **130**, 217 (1997).
9. S. M. Deshpande, *A Second Order Accurate, Kinetic-Theory Based, Method for Inviscid Compressible Flows*, Tech. Paper 2613 (NASA Langley, 1986).
10. D. Drikakis and S. Tsangaris, On the solution of the compressible Navier–Stokes equations using improved flux vector splitting methods, *Appl. Math. Modeling* **17**, 282 (1993).
11. D. Gilbarg and D. Paolucci, The structure of shock waves in the continuum theory of fluids, *J. Ration. Mech. Anal.* **2**, 617 (1953).
12. S. K. Godunov, A difference scheme for numerical computation of discontinuous solutions of hydrodynamic equations, *Math. Sbornik*, **47**, 271 (1959).
13. R. J. Hakkinen, L. Greber, L. Trilling, and S. S. Abarbanel, NASA Memo. 2-18-59W (NASA, 1959).
14. A. Harten, On a class of high resolution total variation stable finite difference schemes, *SIAM J. Numer. Anal.* **21**, 1 (1984).
15. A. Harten, High resolution schemes for hyperbolic conservation laws, *J. Comput. Phys.* **49**, 357 (1983).
16. X. He and L. S. Luo, Lattice Boltzmann model for the incompressible Navier–Stokes equation, *J. Stat. Phys.* **88**, 927 (1997).
17. C. Hirsch, *The Numerical Computation of Internal and External Flows* (Wiley, New York, 1990), Vols. 1 and 2.
18. L. H. Holway, Kinetic theory of shock structure using an ellipsoidal distribution function, Rarefied Gas Dynamics, in *Proceedings of Fourth International Symposium* (1966), vol. 1, pp. 193–215.
19. W. H. Hui and S. Kudriakov, *On Wall Overheating and Other Computational Difficulties of Shock Capturing Methods*, preprint (2001).
20. A. Jameson, W. Schmidt, and E. Turkel, *Numerical Solution of the Euler Equations by Finite Volume Methods using Runge–Kutta Stepping Schemes*, Technical Paper 81-1259 (AIAA Press, Washington DC, 1981).
21. M. Junk and S. V. R. Rao, A new discrete velocity method for Navier–Stokes equations, *J. Comput. Phys.* **155**, 178 (1999).
22. M. N. Kogan, *Rarefied Gas Dynamics* (Plenum, New York, 1969).
23. H. W. Liepmann and A. Roshko, *Elements of Gasdynamics* (Wiley, New York, 1957).
24. T. Lou, D. C. Dahlby, and D. Baganoff, A numerical study comparing kinetic flux vector splitting for the Navier–Stokes equations with a particle method, *J. Comput. Phys.* **145**, 489 (1998).

25. S. H. Lui and K. Xu, Entropy analysis of gas-kinetic schemes for the compressible Euler equations, Z. angew. *Math. Phys.* **52**, 62 (2001).
26. M. N. Macrossan, The equilibrium flux method for the calculation of flows with non-equlibrium chemical reactions, *J. Comput. Phys.* **80**, 204 (1989).
27. J. C. Mandal and S. M. Deshpande, Kinetic flux vector splitting for Euler equations, *Comput. Fluids* **23**, 447 (1994).
28. H. Nessyahu and E. Tadmor, Non-oscillatory central differencing for hyperbolic conservation laws, *J. Comput. Phys.* **87**, 408 (1990).
29. G. N. Patterson, *Molecular Flow of Gases* (Wiley, New York, 1956).
30. B. Perthame, Second-order Boltzmann schemes for compressible Euler equation in one and two space dimensions, *SIAM J. Numer. Anal.* **29**, 1 (1992).
31. K. H. Prendergast and K. Xu, Numerical hydrodynamics from gas-kinetic theory, *J. Comput. Phys.* **109**, 53 (1993).
32. D. I. Pullin, Direct simulation methods for compressible inviscid ideal gas flow, *J. Comput. Phys.* **34**, 231 (1980).
33. R. D. Reitz, One-dimensional compressible gas dynamics calculations using the Boltzmann equations, *J. Comput. Phys.* **42**, 108 (1981).
34. P. Roe, A brief introduction to high-resolution schemes, in *Upwinding and High-resolution Schemes*, edited by M. Y. Hussain, B. van Leer, and J. van Rosendale (Springer, Verlag, New York, 1997).
35. R. H. Sanders and K. H. Prendergast, The possible relation of the three-kiloparsec arm to explosions in the galactic nucleus, *Astrophys. J.* **188**, 489 (1974).
36. J. L. Steger and R. F. Warming, Flux vector splitting of the inviscid gas-dynamic equations with applications to finite difference methods. *J. Comput. Phys.* **40**, 263 (1981).
37. M. D. Su, K. Xu, M. Ghidaoui, Low speed flow simulation by the gas-kinetic scheme, *J. Comput. Phys.* **150**, 17 (1999).
38. H. Z. Tang and K. Xu, Pseudo-particle representation and positivity analysis of explicit and implicit Steger–Warming FVS schemes, *ZAMP*, in press.
39. E. Toro, *Riemann Solvers and Numerical Methods for Fluid Dynamics* (Springer-Verlag, New York, 1999).
40. B. van Leer, Towards the ultimate conservative difference scheme IV, A new approach to numerical convection, *J. Comput. Phys.* **23**, 276 (1977).
41. B. van Leer, *Flux-vector Splitting for the Euler Equations*, Technical Report 82-30 (ICASE, 1982).
42. B. van Leer, J. L. Thomas, P. L. Roe, and R. W. Newsome, *A Comparison of Numerical Flux Formulas for the Euler and Navier–Stokes Equations*, Technical Paper 87-1104 (AIAA Press, Washington, DC, 1987).
43. W. G. Vincenti and C. H. Kruger, Jr., *Introduction to Physical Gas Dynamics* (Wiley, New York, 1965).
44. J. von Neumann and R. D. Richtmyer, A method for the numerical calculation on hydrodynamic shocks, *J. Appl. Phys.* **21**, 232 (1950).
45. P. Woodward and P. Colella, Numerical simulations of two-dimensional fluid flow with strong shocks, *J. Comput. Phys.* **54**, 115 (1984).
46. K. Xu, *Gas-Kinetic Schemes for Unsteady Compressible Flow Simulations*, VKI for Fluid Dynamics Lecture Series 1998-03 (1998).
47. K. Xu, Comments on "Development of an improved gas-kinetic BGK scheme for inviscid and viscous flows," *J. Comput. Phys.*, in press.
48. K. Xu and J. S. Hu, Projection dynamics in Godunov-type schemes, *J. Comput. Phys.* **142**, 412 (1998).
49. K. Xu and Z. W. Li, Dissipative mechanism in Godunov-type schemes, *Int. J. Numer. Meth. Fluids*, in press. Also available at http://www.math.ust.hk/∼makxu.
50. K. Xu and L. S. Luo, Connection between Lattice Boltzmann equation and beam scheme, *Int. J. Modern Physics C* **9**, 1177 (1998).
51. K. Xu, L. Martinelli, and A. Jameson, Gas-kinetic finite volume methods, flux-vector splitting and artificial diffusion, *J. Comput. Phys.* **120**, 48 (1995).
52. K. Xu and K. Prendergast, Numerical Navier–Stokes solutions from gas-kinetic theory, *J. Comput. Phys.* **114**, 9 (1994).
53. K. Xu and H. Z. Tang, *An Explanation for the Sonic Point Glitch*, preprint (2000).